Journal Pre-proof

Mineralogical and geochemical characterization of fossil bones from a Miocene marine Konservat-Lagerstätte

Bosio Giulia, Gioncada Anna, Gariboldi Karen, Bonaccorsi Elena, Collareta Alberto, Pasero Marco, Di Celma Claudio, Malinverno Elisa, Urbina Mario, Bianucci Giovanni

Please cite this article as: Giulia, B., Anna, G., Karen, G., Elena, B., Alberto, C., Marco, P., Claudio, D.C., Elisa, M., Mario, U., Giovanni, B., Mineralogical and geochemical characterization of fossil bones from a Miocene marine Konservat-Lagerstätte, *Journal of South American Earth Sciences* (2020), doi: https://doi.org/10.1016/j.jsames.2020.102924.

This is a PDF file of an article that has undergone enhancements after acceptance, such as the addition of a cover page and metadata, and formatting for readability, but it is not yet the definitive version of record. This version will undergo additional copyediting, typesetting and review before it is published in its final form, but we are providing this version to give early visibility of the article. Please note that, during the production process, errors may be discovered which could affect the content, and all legal disclaimers that apply to the journal pertain.

The corresponding author is Giulia Bosio.

All the authors have contributed equally to the construction of the paper.

1 **Mineralogical and geochemical characterization of fossil bones from a Miocene marine**

2 **Konservat-Lagerstätte**

3

4 Bosio Giulia[1,2]*, Gioncada Anna[1], Gariboldi Karen[1], Bonaccorsi Elena[1], Collareta Alberto[1], Pasero

5 Marco[1], Di Celma Claudio[3], Malinverno Elisa[2], Urbina Mario[4], Bianucci Giovanni[1]

6

7 [1] Dipartimento di Scienze della Terra, Università di Pisa, 56126 Pisa, Italy.

8 giulia.bosio.giulia@gmail.com; anna.gioncada@unipi.it; karen.gariboldi@dst.unipi.it;

9 elena.bonaccorsi@unipi.it; alberto.collareta@unipi.it; marco.pasero@unipi.it;

10 giovanni.bianucci@unipi.it

11 [2] Dipartimento di Scienze dell'Ambiente e della Terra, Università degli Studi di Milano-Bicocca,

12 20126 Milano, Italy. giulia.bosio.giulia@gmail.com; elisa.malinverno@unimib.it

13 [3] Scuola di Scienze e Tecnologie, Università di Camerino, 62032 Camerino, Italy.

14 claudio.dicelma@unicam.it

15 [4] Departamento de Paleontología de Vertebrados, Museo de Historia Natural, Universidad Nacional

16 Mayor de San Marcos, Lima 1, Peru. mariourbina01@hotmail.com

17

20

21 Highlights

22 - Fossil vertebrates from the Pisco-Sacaco Lagerstätte are often exceptionally preserved

23 - Bones differ by color, mineralization degree, chemistry and presence of concretions

24 - Fossil bones from the same Lagerstätte underwent different fossilization paths

25 - Early apatite or dolomite formation mechanisms are crucial for bone preservation

26 - Early diagenetic minerals reduce permeability and limit bone phosphatization

27

28 **Abstract**

29 Fossil bones, together with teeth, are the most common remains of vertebrates that could manage to

30 get preserved over geological times, providing information on the diagenetic and fossilization

31 processes that occurred in the depositional paleoenvironment. Fossil bones from the marine

32 vertebrate Konservat-Lagerstätte in the East Pisco Basin and Sacaco area (Peru) show a high variety

33 of different textural and chemical features, suggestive of different processes variably contributing to

34 the fossilization path. At the macroscopic scale, bone samples can be grouped into six different

35 categories on the basis of the color (red to gray to white) and hardness (which relates to the

36 mineralization degree); a variety of case studies can be found between these categories.

37 Microscopically, the original microstructure of the bone tissue, both compact and cancellous, is well

38 preserved in all the studied samples, with differences in cavity fillings, distribution of microcracks,

39 and presence of Fe oxides in the diverse bone types. The bone composition and mineralogy

40 correspond to fluorapatite. Differences in color, mineralization degree and geochemistry can be

41 interpreted in terms of different fossilization paths, from burial at the seafloor to exposure in the

42 present-day desert environment. The fossilization paths are strongly conditioned by the factors

43 controlling the interplay of the mechanisms of apatite dissolution-recrystallization and dolomite

44 precipitation (formation of carbonate concretions) and the fixation of iron in finely disseminated

45 sulfides in the very early stages of fossilization.

46

47 **1. Introduction**

48   Made of organic and inorganic constituents, bone is a framework of calcium phosphate, similar

49 in composition and structure to the apatite group minerals (hydroxylapatite, $Ca_{10}(PO_4)_6(OH)_2$; in a

50 carbonate-bearing variety $(Ca,Mg,Na)_{10-x}[(PO_4)_{6-x}(CO_3)_x](OH)_{2-x}$), embedded in a protein and lipid

51 matrix (Elliott, 2002; Wopenka and Pasteris, 2005; Pasero et al., 2010; Li and Pasteris, 2014; Fig.

52 1A). Fossil bone forms, with enamel, the fossil remains of vertebrates, and it can resist to decay

53   over geological times, allowing paleontological and paleoecological reconstructions of past

54   environments (Trueman and Tuross, 2002; Keenan, 2016). Due to the high non-mineral content

55   (apatite is only 33-43% by volume, with the rest being made by organics and water, Olszta et al.,

56   2007), important mineralogical, chemical and textural changes affect bones after death in order to

57   permit preservation in the deep time, starting from the early stages after burial (from days to weeks)

58   and continuing for years (Pfretzschner, 2004; Trueman et al., 2004, 2008; Keenan and Engel, 2017).

59   During the early post-mortem history, collagene decay liberates apatite crystallites (Fig. 1B), which

60   are very reactive due to their small size and crystalline structure (Keenan, 2016). Mechanisms of

61   dissolution-recrystallization and increase in size of the apatite crystallites, reducing the surface area

62   to volume ratio, coupled with the transformation of the Ca-phosphate from the original

63   hydroxylapatite into the thermodynamically more stable fluorapatite, favor the preservation of the

64   original bone histology (Elorza et al., 1999; Keenan, 2016). During the late diagenesis, further

65   recrystallization of Ca-phosphate mineral and permineralization of the bone cavities by carbonates,

66   sulfides, iron or manganese oxides, and silica may occur (Pfretzschner, 2004).

67   In the case of marine vertebrates, the post-mortem changes occurring to the fossilized bone tissue

68   over geological timescales depend on a variety of factors, some of which are interdependent (e.g.,

69   the physical and chemical features of the sediment and seawater at the sea bottom and the presence

70   of soft organic matter), while others are totally independent (e.g., the timing of burial and

71   exhumation history). This complex story is recorded in form of the textural, mineralogical and

72   chemical features of both the fossil bones and entombing deposits. Therefore, an assessment of the

73   chemical and mineralogical characteristics of fossil bones and their host sediment can provide

74   information on the geological and fossilization history (Hubert et al., 1996; Herwartz et al., 2013;

75   Trueman, 2013), thus contributing to shed light on the causes behind situations of exceptional

76   preservation (Fossil Konservat-Lagerstätten).

77   The Cenozoic Konzentrat- and Konservat-Lagerstätte of the East Pisco Basin and Sacaco area

78   (Peru) displays exceptional concentrations of fossil marine vertebrates (Esperante et al., 2015;

79 Bianucci et al., 2016a, b), several of which are exquisitely preserved. Examples of that include

80 digestive tract contents of cetaceans, baleen plates of mysticete whales, and skeletons of

81 cartilaginous fishes (Esperante et al., 2008; Ehret et al., 2009, 2012; Collareta et al., 2015, 2017,

82 2020; Gioncada et al., 2016; Lambert et al., 2015; Marx et al., 2017). The richness of the fossil

83 record preserved in this Lagerstätte and its extension over a rather long interval of time and through

84 different sedimentation environments make it an ideal setting for research efforts aimed at

85 understanding how the mineralogy and geochemistry of fossil bones can reflect different

86 fossilization paths and processes. Nevertheless, a mineralogical and chemical study of fossil bones

87 from this outstanding paleontological scenario is still largely lacking. The present work provides

88 new results from field observations and petrographic, mineralogical and geochemical data regarding

89 the bones of marine vertebrates from the Konservat-Lagerstätte of the Pisco-Sacaco Lagerstätte

90 (southern Peru) (Esperante et al., 2015; Bianucci et al., 2016a, b). These results are then discussed

91 with the aim of constraining the fossilization histories of bones displaying different macro- and

92 microscopic features. Our assessment provides new clues for understanding the factors determining

93 the preservation of the fossil marine vertebrates from the Pisco-Sacaco Lagerstätte.

94

2. Geological background

96   The tectonic evolution of Peru has been controlled, since Mesozoic times, by the convergence of

97 the oceanic Nazca/Farallon Plate and the continental South American Plate. In correspondence of

98 this composite transform-convergent margin, normal to strike-slip faults led to the formation of

99 extensional/pull-apart basins along the forearc of Peru (e.g., Kulm et al., 1982; Dunbar et al., 1990;

100 León et al., 2008). Two trench-parallel structural highs formed on the continental shelf and upper

101 slope during the Late Cretaceous and early Paleogene times, i.e., the Outer Shelf High and the

102 Upper Slope Ridge (Thornburg and Kulm, 1981). As a consequence of this, the Peruvian offshore is

103 now segmented into an outer set of slope basins and an inner set of shelf basins (Fig. 2A). The East

104 Pisco Basin is a northwest-southeast elongated shelf basin that extends for ca. 180 km along the

105 southern Peruvian coast between the towns of Pisco and Nazca (Fig. 2A). The East Pisco Basin is

106 placed just landward of where the aseismic Nazca Ridge (a region of topographically high and

107 buoyant oceanic crust) impinges the Peru-Chile trench (Pilger, 1981; Hsu, 1992; Macharé and

108 Ortlieb, 1992; Hampel, 2002) and its fill includes, in ascending stratigraphic order, the Eocene

109 Caballas and Paracas formations, the upper Eocene Otuma Formation, the lower Miocene Chilcatay

110 Formation, and the middle Miocene–Pliocene Pisco Formation (Dunbar et al., 1990; DeVries, 1998,

111 2017; DeVries et al., 2017; DeVries and Jud, 2018; Di Celma et al., 2017, 2018a, b; Solís Mundaca,

112 2018; Coletti et al., 2019). These sedimentary units are compositionally complex and are bounded

113 by regionally extensive unconformities marked by pavements of pebble- to boulder-sized igneous

114 clasts. The unconformities in-between them reflect relatively prolonged periods of subaerial

115 exposure and, as such, they testify to major breaks of the sedimentary history of the East Pisco

116 Basin (DeVries, 1998). As a consequence of this, the local sedimentary succession should be

117 regarded as a series of alloformations (Di Celma et al., 2018a) as defined by the NACSN (2005).

118   Among the sedimentary units exposed in the East Pisco Basin, the Chilcatay and Pisco

119 formations have been recently investigated due to the diverse and exceptionally preserved fossil

120 vertebrate assemblages that were discovered at several sites along the western side of the lower Ica

121 valley (Di Celma et al. 2016a, b, 2018b, 2019; Bianucci et al., 2018). During deposition of these

122 units, the East Pisco Basin was a shallow-marine, semi-isolated embayment, sheltered eastward by

123 a longshore chain of crystalline basement islands (i.e., the so-called "Gran Tablazo Archipelago"

124 *sensu* DeVries and Jud, 2018) (Marocco and Muizon, 1988b; Bianucci et al., 2018). Along the Ica

125 Valley, south of the Ocucaje village, the Chilcatay Formation is comprised of two distinct

126 allomembers, namely, Ct1 and Ct2; the former includes three facies associations, recording

127 deposition in shoreface (*Ct1c*), offshore (*Ct1a*), and subaqueous delta (*Ct1b*) settings, whereas the

128 latter includes two facies associations, recording deposition in shoreface (*Ct2a*) and offshore (*Ct2b*)

129 settings (Di Celma et al. 2018b, 2019). The overlying Pisco Formation is comprised of three fining-

130 upward allomembers, designated P0, P1, and P2 from oldest to youngest, which progressively onlap

131 a composite basal unconformity northeastwards. Each unit, representing a transgressive cycle,

132 recorded deposition in shoreface (sandstones) and offshore (siltstones/diatomaceous siltstones)

133 settings. In this area, the chronostratigraphic framework of the Chilcatay and Pisco formations is

134 well constrained via the integration of micropaleontological data and isotope geochronology.

135 Diatom and silicoflagellate biostratigraphy together with ^{39}Ar–^{40}Ar ages on tephra layers suggest

136 deposition of the Chilcatay strata during the Burdigalian, between 19 and 17 Ma; the lower

137 allomember of the Pisco Formation (P0) is dated at the Langhian-Serravallian by means of

138 strontium isotope stratigraphy, whereas the youngest P1 and P2 allomembers are constrained

139 between 9.5 Ma and 8.6 Ma (Tortonian), and between 8.4 and, at least, 6.7 Ma (Tortonian-

140 Messinian), respectively, thanks to diatom biostratigraphy and ^{39}Ar–^{40}Ar ages (Gariboldi et al.,

141 2017; Di Celma et al., 2018b; Bosio et al., 2020a, b).

142   Sand-prone sediments assigned to the Pisco Formation (DeVries, 2020 and references therein)

143 also crop out in the much smaller Sacaco sub-basin, whose northern edge is encountered about 60

144 km south of Nazca (Fig. 2A). The Sacaco sub-basin (sometimes referred to as the "southern Pisco

145 Basin", e.g., Ehret et al., 2012; Gariboldi et al., 2017) extends for about 50 km along the Peruvian

146 coastline, from Lomas to Yauca (Fig. 2A). Nowadays, it is separated from the East Pisco Basin by a

147 structural high of basement rocks that constitutes the reliefs of Monte Grande and Marcona,

148 southeast of Nazca; so far, however, the tectonic relationships between these two areas of Neogene

149 outcrops are still not clear, and their separation might even have followed the deposition of the

150 Pisco Formation. In the Sacaco area, the chronostratigraphic framework is less clearly defined than

151 in the East Pisco Basin. However, the Pisco-equivalent sediments exposed in this area have been

152 generally regarded as younger than those of the East Pisco Basin exposed in the Ica Valley (e.g.,

153 Muizon and DeVries, 1985; Muizon, 1984, 1988; Marocco and Muizon, 1988a, b; DeVries, 2020).

154 Following a largely biochronological approach, Muizon and DeVries (1985) and Muizon (1988)

155 subdivided the fossiliferous succession of the Sacaco sub-basin in a number of vertebrate-bearing

156 levels defined on the basis of their faunal composition and supported by radiometric ages (Muizon

157 and Bellon, 1980, 1986). Such a framework provided a first rough estimate of the

158 chronostratigraphic asset of the Pisco-equivalent strata in the Sacaco area, whose outcrops were

159 believed to span from the lower upper Miocene (ca. 9 Ma, "El-Jahuay vertebrate level") to the

160 lower Pliocene (ca. 4 Ma, "Sacaco vertebrate level") (Lambert and Muizon, 2013). Each vertebrate-

161 bearing level was originally thought to encompass a single fossiliferous locality, and vice-versa;

162 however, further field work has since clarified that the stratigraphic range of some localities is

163 greater than that of the eponymous vertebrate level (Lambert and Muizon, 2013). Confusion

164 between localities and vertebrate levels has thus arisen in some subsequent works (e.g., Brand et al.,

165 2011). Moreover, U–Pb dating on zircon grains from tuff layers and Sr-isotope analyses on marine

166 mollusk shells provided by Ehret et al. (2012) have suggested that strata exposed in the Sacaco area

167 could be entirely referable to the upper Miocene (late Tortonian – latest Messinian) and, therefore,

168 they seemingly originated during the same time span of the Pisco Formation in the East Pisco

169 Basin.

170

171 **3. Materials and methods**

172   In order to account for the variability of bone preservation styles observed in the field, forty-four

173 fossil cetacean specimens were selected for sampling among those found and described during

174 several field surveys (2015–2019) at the localities of Cerro Colorado (14°21'01''S; 75°53'46''W),

175 Cerro los Quesos (14°29'57''S; 75°43'06''W), Cerro la Bruja (14°31'44''S; 75°39'54''W), Pampa

176 Corre Viento (14°27'S; 75°45'W) and Ullujaya (14°34'59''S; 75°38'27''W) in the East Pisco

177 Basin (Fig. 2B), and Hueso Blanco (15°28'53''S; 74°48'26''W) and Montemar (15°33'28''S;

178 74°45'58''W) in the Sacaco sub-basin (Fig. 2C). Most of these fossil vertebrate specimens have

179 been identified and geolocalized by Bianucci et al. (2016a, b, 2018) and Di Celma et al (2018b). A

180 complete list of the sampled specimens is reported in Table S1.

181   The materials devoted to the analytical investigations include small fragments of bones (mostly

182 rib fragments) and the host sediment (see Table S1). Sampling used the smallest amount of material

183 necessary. Since color and hardness of fossil bones may be indicative of element uptake and apatite

184 recrystallization and/or permineralization, we selected bones with different macroscopic colors and

185 hardness (qualitative evaluation, comparatively estimated) for analytical follow-up. We recorded all

186 the relevant information about the vertebrate specimen, the host sediment, and the exposure to

187 weathering agents (see Table S1 for the complete dataset). In order to distinguish the characteristics

188 related to the pre-exhumation history of the bones from those acquired following the exhumation

189 and exposure to the weathering agents of the present-day desert environment (e.g., wind, sunlight,

190 thermal excursions, night humidity...), we also collected exposed bones, avoiding bones with

191 evidence of transport and reworking.

192   Twenty thin sections were prepared for petrographic investigations under the microscope, in both

193 transmitted and reflected light. Bone fragments were embedded in epoxy resin and cut with a

194 diamond saw. After cutting, bone slices were covered again with epoxy resin in order to fill all the

195 empty spaces of the porous structure of the bone, and an UV resin was used for gluing the glass.

196 Thin sections were then polished with silicon carbide and alumina.

197   The microanalytical investigations focused on the compact (cortical) portion of the bone (Fig.

198 1A). For each bone type (see below), fragments of the compact bone were mounted in epoxy,

199 sectioned orthogonal to the bone elongation, and polished for scanning electron microscopy (SEM)

200 and electron dispersion spectroscopy (Philips XL30 SEM equipped with DX4i EDAX

201 microanalysis, Università di Pisa) aimed at describing their microstructural features and elemental

202 composition, and for electron microprobe analysis (EPMA Cameca SX50, CNR, Rome) aimed at

203 obtaining their chemical composition in terms of major and minor elements. SEM images were

204 collected by using both secondary electrons (SE) and backscattered electrons (BSE). The SEM-EDS

205 analytical conditions were 20 kV accelerating voltage, 5 nA beam current and 10 mm working

206 distance. EPMA analytical conditions were 15kV accelerating voltage, 5 nA beam current, and a

207 10-micron defocused beam was used. Analysis of a reference apatite standard is provided in Table

208 S2 of the Supplementary Material.

209   Fragments of the cortical part of four bones were visually checked under a stereomicroscope to

210   eliminate both the exterior of the bone and any sediment clast. The bone fragments were

211   subsequently powdered and treated with nitric and fluoridric acid digestion procedure for

212   inductively coupled plasma mass spectrometry (ICP-MS) analyses. The concentrations of 35 trace

213   elements were determined by using a Perkin Elmer NexION 300x spectrometer at the Università di

214   Pisa. RGM-1 and JB-2 reference materials were also analyzed.

215   X-ray diffraction (XRD) analyses were carried out at the Università di Pisa. XRD analyses were

216   performed with a Bruker D2 Phaser diffractometer, operating at 10 mA and 30 kV. Data were

217   processed using the software DIFFRAC.EVA V4.1 for identifying the mineralogical phases.

218   The host sediment or rock was inspected with a stereomicroscope and examined via SEM-EDS;

219   representative samples of different host rock types were analyzed by means of ICP-MS as described

220   above.

221

222   **4. Results**

223   *4.1. Field observations and bone macroscopic characteristics*

224   In this work, we examined Miocene vertebrate remains of cetaceans (both odontocetes and

225   mysticetes), which are the most represented group in the Neogene fossil record of the East Pisco

226   Basin and Sacaco sub-basin (e.g., Muizon and DeVries, 1985; Brand et al., 2011; Bianucci et al.,

227   2016a, b, 2018), and a few pinnipeds (see Table S1 for the complete dataset). The fossil remains of

228   these marine vertebrates display a wide range of preservation degrees and modes. From a

229   taphonomic point of view, the vertebrates exhibit different degrees of skeletal completeness,

230   ranging from the preservation of more than 75% of the skeletal elements (e.g., Fig. 2D and type 2 in

231   Fig. 3, see Table S1) to the preservation of a single skeletal element (see types 4, 5, 6 in Fig. 3). The

232   skeletons also show different degree of articulation, ranging from 100% of articulated bones (e.g.,

233   Fig. 2D and types 1, 2, 3 in Fig. 3; see also Table S1) to fully disarticulated bones (see types 4, 5, 6

234   in Fig. 3, and Table S1).

235   The fossil remains are embedded in different kinds of variably lithified sediments, including

236   diatomaceous mudstones and siltstones, volcanogenic or terrigenous siltstones, and fine- to coarse-

237   grained sandstones. In some cases, the fossils are entombed within a hard, massive, tightly-

238   cemented rock formed by carbonate concretions (i.e., a framework of diatom and/or terrigenous

239   clasts cemented by Ca-Mg-carbonate), the latter being mostly represented by dolomite nodules as

240   described by Gariboldi et al. (2015) (e.g., type 1 of Fig. 3). The sediment or rock surrounding the

241   non-exposed fossil bones exhibits, till a distance of a few to ca. 30 centimeters from the bone

242   surface, a color that differs from the rest of the sediment, being intensely reddened (see type 2 of

243   Fig. 3) and sometimes delimited by an evident dark boundary that develops within a yellowish

244   sediment (see type 3 of Fig. 3). This sequence, resulting from an enrichment in Fe in the red layer

245   and in Mn in the black ones, corresponds to the yellow–black–red (YBR) sequence described by

246   Gariboldi et al. (2015) and Gioncada et al. (2018a) in the sediments hosting the bone remains.

247   Based on differences in macroscopic color (dark amber, red, pearly white, white/pinkish, dark

248   gray, white/gray-white) and hardness, bone samples were grouped into six different categories,

249   which are described in Table 1 and illustrated in Figure 3. The white/pinkish bones of type 1 (Fig.

250   3) are usually fragile and easily crumbling, with the bone tissue exhibiting a low hardness, and they

251   are embedded in a complete (type 1a) or partial (type 1c) dolomite nodule, or in volcanic ashes

252   (type 1b). Red-colored, moderately hard bones in a loose silty/sandy sediment characterize type 2

253   (Fig. 3). Bones of type 3 are dark amber in color (Fig. 3), moderately hard, and hosted in scarcely

254   cemented silty/sandy sediments made of diatoms and terrigenous (volcanoclastic) clasts. The pearly

255   white, moderately hard bones are grouped in the type 4, whereas the white/gray-white and hard

256   bones constitute type 5 (Fig. 3). Both types do not exhibit concretions and are hosted in Ca-

257   carbonate-bearing clastic siltstones. Finally, bones of type 6, represented by only one sample,

258   display the highest values of hardness in our dataset, a dark gray color (Fig. 3), and they are hosted

259   in a loose siliciclastic sediment.

260

261 *4.2. Petrography and SEM-EDS results*

262   When observed under the transmitted light optical microscope, bone color ranges from colorless

263 to red or reddish brown (Fig. 4). Bones of the type 2, displaying a red color in hand samples, retain

264 a variably red to orange color also under the microscope (Fig. 4G, H). The red color of the bone

265 tissue is usually associated to the presence of abundant Fe-oxides lining or partially filling the

266 intertrabecular medullary cavities and interspersed in the sediment adjacent to the bone (opaques in

267 Fig. 4G, H).

268   The original microstructure of the compact bone tissues is well preserved in all samples and not

269 noticeably modified by permineralization. Bone tissues preserve the microstructure with the

270 osteocyte lacunae and lamellae being identifiable in all the six bone types; they are particularly

271 well-preserved in types 4, 5 and 6, and well to poorly preserved in types 1 and 2 (Fig. 4A, B).

272 Microcracks through the bone tissue are uncommon; in some cases, they can be observed radially

273 distributed from the Haversian canals outwards. Only in type 6, the hardest one, the bone tissue

274 displays pervasive cracks, distributed independently from the histological microstructure of the

275 bone (Fig. 4C).

276   As regards the bone tissue composition, the EDS spectra indicate that it is Ca-phosphate.

277 Different average atomic weight in the different bone types is revealed by the grayscale of the BSE

278 imaging (Fig. 5), which indicates different degrees of mineralization (Bloebaum et al., 1997). This

279 is particularly evident in the difference observed between types 1 and 6 (Fig. 5A, E). Such an

280 observation corresponds to the macroscopic evaluation of the white/pinkish bones as the softest and

281 least mineralized type, and the dark gray bones as the hardest and most mineralized (Table 1). In

282 type 4, the bone tissue appears more mineralized than in type 1 (Fig. 5B, C), and the Haversian

283 canals are partially filled by newly precipitated apatite (Fig. 5D). The type 2 red-colored bones

284 display a similar mineralization degree (Fig. 5F).

285   Bone cavities, i.e. the Haversian canals in the cortical bone and intertrabecular medullary

286 cavities in the cancellous bone, might exhibit a partial or complete filling by various minerals,

287 besides the above reported apatite (Fig. 5D), formed at different stages through early and late

288 diagenesis. These are dolomite, iron and manganese oxides, calcite, gypsum/anhydrite.

289 Iron oxides can be found both in osteocyte lacunae and canaliculi (Fig. 4C inset), and/or lining

290 intertrabecular medullary cavities (Fig. 4G, H). The opaque iron oxides filling osteocyte lacunae

291 and canaliculi (Fig. 4C inset) typically testify the early formation of pyrite due to reducing

292 conditions for the presence of decaying organic material (Pfretzschner, 2001a).

293 Micro- and cryptocrystalline dolomite can be found adjacent to the bone and filling also the

294 microborings in the bone cortical tissue, the Haversian canals and the intertrabecular medullary

295 cavities, in association to variable amounts of finely disseminated iron oxides (Fig. 4D; 6A, B, C).

296 Such a carbonate occurrence and association with iron oxides, the latter being morphologically

297 reminiscent of relics of pyrite framboids (Fig. 6C), represent evidence of the sulfate-reducing

298 bacterial metabolic activity consequent to the decay of the organic matter in the carcass (Gariboldi

299 et al., 2015; Gioncada et al., 2016, and references therein). Therefore, dolomite and iron oxides

300 formed very early.

301 Following this interpretation, the micro- and cryptocrystalline carbonates testify to an incipient

302 development of dolomite concretions similar to those described by Gariboldi et al. (2015) from the

303 sediment entombing marine vertebrate skeletons of the Pisco Formation. In several cases, sediment

304 particles (diatoms, terrigenous minerals) are present inside the bone cavities (Fig. 4E), being often

305 separated from the bone by a thin, early-formed dolomite layer (Gariboldi et al. 2015). These

306 sediment particles entered with seawater, possibly sucked in by the outgoing gas bubbles originated

307 by decomposing organic matter (Bodzioch, 2015), and were then quickly cemented by the ongoing

308 processes of dolomite formation. In some cases, the presence of sediment can be interpreted as

309 clasts entering broken bones exposed at the seafloor before burial.

310 Both in the presence of the dolomite concretions and in absence of them, the residual porosity is

311 in some cases filled by mineral phases displaying microcrystalline or coarse mosaic texture, or

312 forming crystals with euhedral terminations in vug-like cavities (Fig. 4B, F; 6D). These are sparry

313 calcite, Ca-sulphates (gypsum/anhydrite), and halite. While sulphates and halite are ubiquitous,

314 calcite is common in the Chilcatay Formation at Ullujaya but extremely rare in the Pisco Formation

315 at the localities of Cerro los Quesos and Cerro Colorado. When carbonates and sulphates coexist,

316 textural evidence indicates that the sulphates postdate the carbonates (Fig. 6D).

317

318 *4.3. X-rays diffractometry and major element chemical composition*

319 The results of the XRPD analyses on the compact bone of the studied samples indicate the

320 presence of apatite and minor anhydrite, dolomite and quartz. Only in type 2 (red) bones the results

321 reveal the presence of goethite. The results of the EPMA analyses of the bone tissue in the studied

322 samples give an F-rich Ca-phosphate composition (Table 2 and Fig. 7). The analytical totals are in

323 the range 85-94 wt% for most bone types, with types 1, 4 and 5 showing scattered values down to

324 80 wt% at constant Ca/P ratios. The values of the microprobe totals are < 100 wt% due to the

325 carbonate and hydroxyl groups in apatite mineral, which are not measured by electron microprobe,

326 as well as to the low compactness (variable degree of mineralization) of the analyzed bone types

327 (Fig. 7A).

328 The Ca/P atomic ratio broadly ranges from 1.3 to 2.1, with clustered values for each bone type

329 with the exception of type 3 (Table 2; Fig. 7B). The Ca/P range embraces the hydroxylapatite

330 mineral stoichiometric value and the range of published bioapatite bone materials (Ca/P= 1.67–

331 1.78; Li and Pasteris, 2014; Wopenka and Pasteris, 2005). The highest Ca/P values are found in

332 type 6 and are due to a gain in Ca rather than to a depletion of P. A contamination by Ca-carbonate

333 cannot be excluded. Among the six categories in which bones were classified based on color and

334 hardness, the dark amber (type 3) and red (type 2) bones have lower Ca/P ratios, and they exhibit

335 higher Si, Fe and Mn abundances as well as lower F abundances than the whitish or gray ones (Fig.

336 7C, D, E, F; Table 2). The iron and silicon content, in particular, are higher in the bone type 2

337 (Table 2, S2, Fig. 7D), also in comparison with extant analyzed whale bones (Decrée et al., 2018).

338 The Fe and Si contents are also quite high in the dark amber-colored phocid specimen of bone type

339 3 (Table 2, S2, Fig. 7D). The red color and the abundant iron oxides (goethite in XRPD analysis) in

340 type 2 bones suggest that the high iron content measured with EPMA could be also the result of a

341 contamination of the analyses by fine iron hydroxides in the bone tissue microporosity.

342

343 *4.4. Trace element geochemistry*

344 Four samples of well-preserved fossil bones, representative of different situations in terms of

345 development of concretions and mineralization degrees of the bone tissue (see Table 1), and four

346 samples of sediment were selected for the trace element analysis. The bone samples are: CC-M63 of

347 the type 1a, within a dolomite nodule; CLQ-M3 of the type 1b, without nodule but with a Mn-Fe

348 boundary layer; CC-M28 of the type 2, strongly mineralized, without nodule but with a Mn-Fe

349 boundary layer, exhibiting Fe enrichment; and MT-M1 of the type 6: strongly mineralized, without

350 nodule, without Fe enrichment.

351 The redox-sensitive elements Cu, Fe, U vary in abundance among the different bone types

352 (Table 3). In particular, U is present with comparatively higher values in specimens MT-M1 of type

353 6 (250 ppm) and CC-M28 of type 2 (45 ppm). Ni (121 ppm), Zn (451 ppm), and Mo (30 ppm) are

354 comparatively higher in the bone sample with the highest Fe content (CC-M28 of the type 2), with

355 values that are higher than those reported for extant marine mammals (Decrée et al. 2018).

356 The REE content of the analyzed bones is $\Sigma REE = 6–60$ ppm, in the lower range of fossil bone

357 REEs (1–10,000 ppm) but remarkably higher than the bone REE concentrations in living

358 organisms, ranging from 0.001 to 1 ppm (Trueman and Tuross, 2002). The REE patterns, reported

359 in Figure 8 after normalization to the PAAS, are variably fractionated, with high HREE up to

360 PAAS-normalized values >1, and low La_N/Yb_N ratio except for the bone sample from within a

361 dolomitic nodule, in which the La_N/Yb_N ratio equals 0.8. Overall, the samples display La_N/Sm_N and

362 La_N/Yb_N ratios close to the field of seawater (Fig. 9). All the samples exhibit a positive Gd anomaly

363 and positive Y peak. In turn, the Ce anomaly is low or absent.

364

365 **5. Discussion**

366 *5.1. Processes of mineralization responsible of bone fossilization in the Pisco-Sacaco Lagerstätte*

367   The studied fossil bone samples display a broad variability of color and hardness values and,

368 based on these, have herein been grouped into six different categories, exhibiting different physical

369 and chemical characteristics. Overall, these different groups depict a continuum of different

370 macroscopic aspects of the bone that can be found in different fossil specimens or even within a

371 same fossil specimen.

372   In the studied samples, the bone tissue consists of Ca-phosphate and no examples of substitution

373 of apatite by other phases (e.g., crystalline or amorphous silica or pyrite) has been detected.

374 Carbonates, iron sulphides and Ca-sulphates formed at different stages, and in the red-colored bones

375 the bone tissue is permeated with minute Fe-oxides (e.g., the brighter areas in Figure 5F), but none

376 of these minerals remarkably replaced the original biogenic apatite. Therefore, both the hardness of

377 the studied fossil bones and the preservation degree of the histological structures must depend on

378 the degree of apatite recrystallization (Fig. 1B), whereas color must depend on element uptake from

379 the local environment and fine iron sulfides precipitation. These mechanisms, on their hand, are

380 influenced by the chemical-physical conditions of porewater (oxygen level, availability of P, Fe, S,

381 Mn) during the very early stages of the fossilization history (pre-burial and burial stages, Fig. 10),

382 which determine the element availability and the nature of the newly formed minerals.

383   Sea floor oxygen availability, abundance of organic matter, and sediment permeability and

384 composition are crucial factors controlling the mineral formation in early diagenesis, immediately

385 after burial (Fig. 10). With respect to the Pisco-Sacaco Lagerstätte vertebrates, the marine sediments

386 in which the carcasses were buried are variably permeable, potentially allowing chemical exchange

387 between the bone and seawater shortly after burial. The least permeable lithologies are the thin,

388 fine-grained tephra layers. Therefore, the aerobic oxidation of the organic matter could be favored.

389 However, the oxygen level at the seafloor was low and occasionally very low (suboxic to anoxic

390 conditions), especially in the offshore environment, as a consequence of the abundant decaying

391 organic matter made available by high productivity waters, and due to the limited circulation of

392 waters in the East Pisco Basin (Bianucci et al., 2018). The Miocene situation was probably similar

393 to that observed in the present-day Peruvian and Chilean slope (Manheim et al., 1975; Rhoads et al.,

394 1991; Emeis et al., 1991; Böning et al., 2004) and in protected bays of the currently submerged

395 portions of the East Pisco Basin (i.e., the Paracas Bay, Aguirre-Velarde et al., 2019). Just below the

396 sediment-seawater boundary, the low O_2 availability and the abundance of organic matter provided

397 by the buried vertebrate carcasses could activate processes of Fe, Mn and sulphate reduction (SBR)

398 shortly after burial (Allison, 1988; Briggs, 2003; Shapiro and Spangler, 2009). The microbial or

399 inorganic reduction of Fe and Mn oxyhydroxides liberates into the porewater the surface-bound

400 phosphate subtracted from the water column (Creveling et al., 2014). Coupled with the phosphorous

401 addition provided by the decay of the organic matter, this P availability promotes the Ca-phosphate

402 mineral recrystallization thanks to the lowering of pH within the apatite dissolution-recrystallization

403 window due to the first products of organic matter decay (Berna et al., 2004). The stability of

404 apatite depends on P availability, pH and the type of phosphate mineral, being carbonate-bearing F-

405 apatite more stable than hydroxylapatite in slightly acidic and low P solutions (Keenan, 2016).

406 Thus, bone preservation is highly dependent on this early process of apatite recrystallization and

407 bone phosphatization (Fig. 1B).

408 On the other hand, bacterial sulfate reduction increases both the abundance of bicarbonate ions

409 and pH, favoring carbonate minerals formation; at the same time, it lowers sulfate concentration, an

410 inhibiting factor for dolomite stability, thus triggering the precipitation of dolomite (Allison, 1988;

411 Briggs and Wilby, 1996; Shapiro and Spangler, 2009; Gariboldi et al., 2015; Gioncada et al.,

412 2018b). At a very early stage, a crucial role is, therefore, played by the chemical-physical properties

413 of porewater for what concerns the conditions favoring Ca-phosphate formation (and bone

414 mineralization) and/or carbonate cement formation (and thus development of dolomite concretions

415 around the bones). Both these processes are pivotal for bone preservation because they may occur

416 very early, and even during the syn-burial stage (Fig. 10), while the organic matter is decomposing

417 (Meister et al., 2011; Muramiya et al., 2020). They affect preservation in a complex way: while the

418 rapid decrease of permeability induced by the early concretion formation limits the decay of organic

419 matter by slowing the interaction with the oxidants (McCoy et al., 2015), it may also limit the

420 availability of P for apatite recrystallization and bone phosphatization. Thus, it can be envisaged

421 that the early formation of concretions (Fig. 10) demonstrated at Cerro Colorado and Cerro los

422 Quesos rapidly reduced the permeability necessary for element uptake from porewater, which

423 limited phosphatization, and as such, bone mineralization (Gariboldi et al. 2015). Bone

424 mineralization by Ca-phosphate is, indeed, found to be higher in samples without the early dolomite

425 concretion (Gioncada et al., 2018a).

426   Given the above described framework, the characteristics of the studied bones provide

427 information on the spectrum of processes controlling the degree of apatite recrystallization, element

428 uptake, and mineral precipitation from porewater that occurred during the early diagenesis, the late

429 diagenesis and the much later exposure in the present-day desert environment. Figure 10

430 summarizes these processes and the factors controlling them, while Figure 11 displays the proposed

431 connection between the variety of characteristics displayed by the fossil bones and the processes

432 they encountered. Carbonate nodules formed very early, and their presence indicates that the

433 fossilization conditions changed rapidly from those favorable for apatite recrystallization to those

434 favorable for nucleation of carbonates; the bones retain a white-pinkish color (type 1, Fig. 11), and

435 are fragile and prone to break. Bones preserved in a sediment without nodule may have been subject

436 to a prolonged apatite recrystallization, providing a dark amber color and a moderate hardness to the

437 bone tissue (type 3, Fig. 11). Bones can acquire an intense red color due to Fe-hydroxides

438 permeating the bone tissue. Iron precipitates as pyrite framboid precursors within the sediment and

439 the bone cavities under reducing conditions in the early stages of the organic matter decay and

440 diagenesis, as a by-product of the Fe and sulfate reduction mechanisms (Pfretzschner, 2000b,

441 2001a; Vietti et al., 2015), and it is then fixed in form of hydroxides following oxidation

442 (Pfretzschner, 2001b) (goethite in type 2, Fig. 11). Mn may also precipitate at redox or pH

443 boundaries. During the late diagenesis, secondary minerals, such as carbonates, anhydrite and

444 halite, precipitated and filled the bone cavities. In type 6 (Fig. 11), the high hardness of the bone is

445 accompanied by both a high Ca content of the bone tissue and a pervasive precipitation of large-

446 sized calcite crystals in the osteons and intertrabecular medullary cavities. Pervasive polygonal

447 microcracks through the bone tissue, preceding the calcite filling, are ascribed to the external

448 stresses in the late diagenetic phase, whereas the radially distributed microcracks around the osteons

449 are to be ascribed to the early diagenetic phase (Pfretzschner, 2000a, 2004). Finally, during the

450 exposure in the present-day desert environment, fossil bones can be bleached and weakened by

451 exogenous agents removing the fine iron oxides and changing their color, resulting in pearly white

452 to gray, moderately hard bones (types 4 and 5, Fig. 11).

453

454 *5.2 Chemical-physical conditions of the fossilization stages*

455   The bones of marine vertebrates of the Pisco Formation consist of fluorapatite and are not

456 affected by relevant processes of permineralization by minerals other than Ca-phosphate.

457 Differences in the totals of microprobe analyses, in Ca/P values, and in Fe and Si contents indicate,

458 however, the existence of diverse compositions in the analyzed bones (Fig. 7). Remarkable

459 differences are also highlighted by the trace element contents in U, Zn, Ni, and REE revealed by

460 four of the studied bones (Fig. 8, Table 3).

461   The higher values of U are to be attributed to enrichment during diagenesis, in the presence of

462 reducing solutions in which U is soluble (Pfretzschner, 2000b; Keenan et al., 2015). Ni, Zn and Mo

463 are comparatively higher in the bone sample with higher Fe contents, which suggests that the

464 sediment hosting the bones was enriched in these elements during sedimentation in oxic conditions,

465 because Ni and Zn are adsorbed onto Fe-Mn particles that form in oxic seawater. Similarly, these

466 particles scavenge from seawater also REE, in particular LREE (Light REE) (Trueman and Tuross,

467 2002; Keenan et al., 2015).

468   During fossilization, REE are taken by the newly formed apatite as substitutes for Ca (Trueman

469   and Tuross, 2002). Firstly, REE uptake depends, therefore, on the composition, pH and redox

470   conditions of the porewater during early diagenesis. On the other hand, the final REE patterns are

471   the result of the long-term diffusion in fossil bones and depend, therefore, on the late diagenetic

472   stages (Herwartz et al., 2013; Kowal-Linka et al., 2014). Thus, REE patterns may fingerprint the

473   paleoenvironment shortly after burial only if they are not overprinted by later diagenetic,

474   hydrothermal or metamorphic events. In the marine environment, mechanisms that determine

475   fractionation and the final REE patterns of fossil bones are complex, but the most relevant include

476   the preferential LREE sorption on bone apatite crystallites as well as the LREE sorption on reactive

477   Fe-Mn oxides and hydroxides (Chen et al., 2015); the latter instance enhances the HREE mobility,

478   thus allowing the HREE to reach the inner parts of the bone (Herwartz et al., 2013). The REE

479   patterns of bones in Figure 8 indicate low and variable REE uptake. The fractionated patterns of

480   three out of four samples and their Gd and Y anomalies strongly recall the influence of oxic

481   seawater (see the low La/Yb ratio, and the positive La, Gd and Y anomalies of Pacific seawater; De

482   Baar et al., 1985), although the lack of any Ce anomaly suggests conditions similar to seawater at

483   the depth of oxygen minimum, i.e., ca. 150 to 200 m (Fig. 8). This is in agreement with the overall

484   suboxic condition at seafloor in the East Pisco Basin, which could be linked to a high oxygen

485   consumption due to high productivity (see paragraph 5.1) as well as to a scarcely efficient exchange

486   with oxygenated oceanic water due to the basin physiography (as has been recently observed for the

487   extant Paracas Bay; Aguirre-Velarde et al., 2019).

488   Moreover, the similarities with the seawater field in Figure 9 indicate that the bones acquired

489   their REE imprint during early diagenesis of marine sediments and that there is no evidence for

490   prolonged diagenetic or metamorphic processes. Only the bones inside a nodule display a scarcely

491   fractionated pattern: this can be explained with early fossilization occurring in locally anoxic

492   conditions due to anaerobic decay of organic matter that caused sulfate reduction, as well as nitrate

493   and Mn-Fe reduction and uptake of LREE formerly scavenged by Fe-Mn particles. The early

494   diagenetic anoxic (sulfidic) conditions likely resulted by organic matter decay consuming oxygen

495   while exchange with oxic seawater was limited by early burial (Gariboldi et al., 2015; McCoy et al.,

496   2015). The formation of a dolomite nodule reduced permeability and consequently limited later

497   modifications of the REE pattern by oxic seawater. The resulting REE pattern corresponds, in fact,

498   to that developing in a sulfate reduction environment (Fig. 9) (see Kim et al., 2012). However,

499   according to Kim et al. (2012), Fe-reduction would cause a MREE bulge in the porewater pattern

500   that is not visible in our bone pattern. The bone found in sediment rich in volcanic ash has the

501   lowest REE contents, although the pattern is similar to that of seawater. Among the different

502   sediment types hosting the bones of the Pisco Formation, volcanic ash is the least permeable, thus

503   probably limiting prolonged interaction with seawater. All the bones without a nodule retain the

504   pattern of seawater, which suggests REE uptake in oxic-suboxic conditions, with relatively low

505   oxygen availability. The highly porous sediment, such as sandstones, allows bones to exchange

506   with the porewater fluids (Gioncada et al., 2018a). The lack of any Eu anomaly is in agreement with

507   the lack of interaction with high temperature, reducing, chloride-rich hydrothermal fluids (Michard,

508   1989).

509

6. Conclusions

511   The fossil bones of marine vertebrates of the Pisco-Sacaco Lagerstätte witness a broad variety of

512   preservation modes, which at the macroscale reflect into different features such as color, hardness

513   and the presence/absence of embedding carbonate concretions. In many cases, the bone tissue

514   displays well preserved histological details at the microscopic scale, such as osteocyte lacunae and

515   lamellae, revealing that processes of phosphatization were active along with the decay of the

516   organic part of the bone tissue during the earliest steps of diagenesis. This prevented the later access

517   of fluids which could favor bone substitution by diagenetic minerals other than apatite. Fe-oxide

518   framboids (former iron sulfides) and microcrystalline dolomite are also early diagenetic minerals.

519   Red-colored bones exhibit abundant Fe oxides in the intertrabecular medullary cavities, preceding

520 late diagenetic minerals and therefore indicating abundant iron sulfide formation during early

521 diagenesis, also within the bone tissue microporosity. Finally, late minerals such as

522 gypsum/anhydrite and halite may partially fill cracks and bone cavities, irrespective of the presence

523 or absence of external dolomite concretions.

524   In absence of dolomite nodule, the siliciclastic sands or silts in which bones are deposited

525 constitute a highly permeable environment where bones can react and exchange elements with the

526 porewater fluids. As a consequence of this, they record a trace element and REE pattern similar to

527 seawater. On the other hand, bones deposited within volcanic ashes or embedded into early

528 diagenetic dolomite nodules experience low permeability conditions, limiting the trace elements and

529 REE uptake.

530   Our data indicate that two main mineral formation mechanisms, both active in the early

531 diagenetic stages, appear to have controlled the mineralization and preservation of the bone tissue

532 during fossilization, namely, the dissolution-recrystallization of apatite and the development of a

533 dolomite concretion enclosing the bone. The macroscopic color of the bone before exposure to

534 weathering is mainly connected to oxidation of early diagenetic iron sulfides.

535   The herein results indicate that future works on bones might hopefully shed new light on the

536 correlation between the physical and chemical characteristics of the bones and their fossilization

537 paths. Bone preservation is determined by independent and interdependent factors and agents that

538 act at different times, and it ultimately reflects the early fossilization, sheltering, and late post-

539 mortem history.

540

545 discussions on marine vertebrates. The authors wish to thank two anonymous reviewers and the

546 Editor F. J. Vega for their useful and constructive comments.

547

548 **Funding**

552

553 **References**

554 Aguirre-Velarde, A., Thouzeau, G., Jean, F., Mendo, J., Cueto-Vega, R., Kawazo-Delgado, M.,

555 Vásquez-Spencer, J., Herrera-Sanchez, D., Vega-Espinoza, A., Flye-Sainte-Marie, J., 2019. Chronic

556 and severe hypoxic conditions in Paracas Bay, Pisco, Peru: Consequences on scallop growth,

557 reproduction, and survival. Aquaculture, 512, 734259.

558 https://doi.org/10.1016/j.aquaculture.2019.734259.

559 Allison, P.A., 1988. The Role of Anoxia in the Decay and Mineralization of Proteinaceous Macro-

560 Fossils. Paleobiology, 14, 2, 139–154.

561 Berna, F., Matthews, A., Weiner, S., 2004. Solubilities of bone mineral from archaeological sites:

562 the recrystallization window. Journal of Archaeological Science, 31, 867–882.

563 Bianucci, G., Collareta, A., Bosio, G., Landini, W., Gariboldi, K., Gioncada, A., Lambert, O.,

564 Malinverno, E., Muizon, C. de, Varas-Malca, R., Villa, I.M, Coletti, G., Urbina, M., Di Celma, C.,

565 2018. Taphonomy and palaeoecology of the lower Miocene marine vertebrate assemblage of

566 Ullujaya (Chilcatay Formation, East Pisco Basin, southern Peru). Palaeogeography

567 Palaeoclimatology Palaeoecology, 511, 256–279. https://doi.org/10.1016/j.palaeo.2018.08.013.

568 Bianucci, G., Di Celma, C., Collareta, A., Landini, W., Post, K., Tinelli, C., Muizon, C. de, Bosio,

569 G., Gariboldi, K., Gioncada, A., Malinverno, E., Cantalamessa G., Altamirano-Sierra, A, Salas-

570   Gismondi, R., Urbina, M., Lambert, O., 2016a. Fossil marine vertebrates of Cerro Los Quesos:

571   Distribution of cetaceans, seals, crocodiles, seabirds, sharks, and bony fish in a late Miocene

572   locality of the Pisco Basin, Peru. Journal of Maps, 12, 1037–1046.

573   https://doi.org/10.1080/17445647.2015.1115785.

574   Bianucci, G., Di Celma, C., Landini, W., Post, K., Tinelli, C., Muizon, C. de, Gariboldi, K.,

575   Malinverno, E., Cantalamessa, G., Gioncada, A., Collareta, A., Salas-Gismondi, R., Varas-Malca,

576   R.M., Urbina, M., Lambert, O., 2016b. Distribution of fossil marine vertebrates in Cerro Colorado,

577   the type locality of the giant raptorial sperm whale Livyatan melvillei (Miocene, Pisco Formation,

578   Peru). Journal of Maps, 12, 543–557. https://doi.org/10.1080/17445647.2015.1048315, 2016b.

579   Bloebaum, R.D., Skedros, J.G., Vajda, E.G., Bachus, K.N., Constantz, B.R., 1997. Determining

580   mineral content variations in bone using backscattered electron imaging. Bone, 20, 485–490.

581   https://doi.org/10.1016/S8756-3282(97)00015-X.

582   Bodzioch, A., 2015. Idealized Model of Mineral Infillings in Bones of Fossil Freshwater Animals,

583   on the Example of Late Triassic Metoposaurs from Krasiejów (Poland). Austin Journal of Earth

584   Science, 2(1), 1008.

585   Böning, P., Brumsack, H.J., Böttcher, M.E., Schnetger, B., Kriete, C., Kallmeyer, J., Borchers, S.L.,

586   2004. Geochemistry of Peruvian near-surface sediments. Geochimica et Cosmochimica Acta, 68,

587   21, 4429–4451.

588   Bosio, G., Malinverno, E., Collareta, A., Di Celma, C., Gioncada, A., Parente, M., Berra, F., Marx,

589   F.G., Vertino, A., Urbina, M., Bianucci, G., 2020a. Strontium Isotope Stratigraphy and the

590   thermophilic fossil fauna from the middle Miocene of the East Pisco Basin (Peru). Journal of South

591   American Earth Sciences, 97, 102399. https://doi.org/10.1016/j.jsames.2019.102399.

592   Bosio, G., Malinverno, E., Villa, I.M., Di Celma, C., Gariboldi, K., Gioncada, A., Barberini, B.,

593   Urbina, M., Bianucci, G., 2020b. Tephrochronology and chronostratigraphy of the Miocene

594   Chilcatay and Pisco formations (East Pisco Basin, Peru). Newsletters on Stratigraphy, in press.

595   https://doi.org/10.1127/nos/2019/0525.

596   Brand, L.R., Urbina, M., Chadwick, A., DeVries, T.J., Esperante, R., 2011. A high resolution

597   stratigraphic framework for the remarkable fossil cetacean assemblage of the Miocene/Pliocene

598   Pisco Formation, Peru. Journal of South American Earth Sciences, 31, 414–425.

599   https://doi.org/10.1016/j.jsames.2011.02.015.

600   Briggs, D.E.G., 2003. The Role of Decay and Mineralization in the Preservation of Soft-Bodied

601   Fossils. Annual Review of Earth and Planetary Sciences, 31, 275–301.

602   https://doi.org/10.1146/annurev.earth.31.100901.144746.

603   Briggs, D.E.G., Wilby, P.R., 1996. The role of the calcium carbonate-calcium phosphate switch in

604   the mineralization of soft-bodied fossils. Journal of the Geological Society, 153, 665–668.

605   Chen, J., Algeo, T. J., Zhao, L., Chen, Z. Q., Cao, L., Zhang, L., Li, Y., 2015. Diagenetic uptake of

606   rare earth elements by bioapatite, with an example from Lower Triassic conodonts of South China.

607   Earth-Science Reviews, 149, 181–202. http://dx.doi.org/10.1016/j.earscirev.2015.01.013

608   Coletti, G., Bosio, G., Collareta, A., Malinverno, E., Bracchi, V., Di Celma, C., Basso, D.,

609   Stainbank, S., Spezzaferri, S., Cannings, T., Bianucci G., 2019. Biostratigraphic, evolutionary, and

610   paleoenvironmental significance of the southernmost lepidocyclinids of the Pacific coast of South

611   America (East Pisco Basin, southern Peru). Journal of South American Earth Sciences, 96, 102372.

612   https://doi.org/10.1016/j.jsames.2019.102372.

613   Collareta, A., Landini, W., Chalcatana, C., Valdivia, W., Altamirano-Sierra, A., Urbina- Schimtt,

614   M., Bianucci, G., 2017. A well preserved skeleton of the fossil shark *Cosmopolitodus hastalis* from

615   the late Miocene of Peru, featuring fish remains as fossilized stomach contents. Riv. Ital. Paleontol.

616   Stratigr. 123, 11–22.

617 Collareta, A., Landini, W., Lambert, O., Post, K., Tinelli, C., Di Celma, C., Panetta, D., Tripodi,

618 M., Salvadori, P.A., Caramella, D., Marchi, D., Urbina, M., Bianucci, G., 2015. Piscivory in a

619 Miocene Cetotheriidae: first record of fossilized stomach content for an extinct baleen-bearing

620 whale. Sci. Nat. 102 article #70.

621 Collareta, A., Tejada-Medina, L., Chacaltana-Budiel, C., Landini, W., Altamirano-Sierra, A.,

622 Urbina-Schmitt, M., Bianucci, G. 2020. A rhinopristiform sawfish (genus *Pristis*) from the middle

623 Eocene (Lutetian) of southern Peru and its regional implications. Carnets Geol., 20(5), 91–105.

624 Creveling, J. R., Johnston, D. T., Poulton, S. W., Kotrc, B., März, C., Schrag, D. P., Knoll, A. H.

625 2014. Phosphorus sources for phosphatic Cambrian carbonates. GSA Bulletin, 126(1-2), 145–163.

626 De Baar, H.J., Bacon, M.P., Brewer, P.G., Bruland, K.W., 1985. Rare earth elements in the Pacific

627 and Atlantic Oceans. Geochimica et Cosmochimica Acta, 49, 1943–1959.

628 https://doi.org/10.1016/0016-7037(85)90089-4.

629 Decrée, S., Herwartz, D., Mercadier, J., Miján, I., de Buffrénil, V., Leduc, T., Lambert, O. 2018.

630 The post-mortem history of a bone revealed by its trace element signature: The case of a fossil

631 whale rostrum. Chemical Geology, 477, 137–150.

632 DeVries, T.J., 1998. Oligocene deposition and Cenozoic sequence boundaries in the Pisco Basin

633 (Peru). J. South Am. Earth Sci. 11, 217–231. https://doi.org/10.1016/S0895-9811(98)00014-5.

634 DeVries, T.J., 2017. Eocene stratigraphy and depositional history near Puerto Caballas (East Pisco

635 Basin, Peru). Boletín de la Sociedad Geológica del Perú, 112, 39–52.

636 DeVries, T.J., 2020. Lithostratigraphy and biostratigraphy of Pliocene and Pleistocene marine

637 deposits and age of the highest marine terrace from the Sacaco Basin and its environs (southern

638 Peru). Boletín de la Sociedad Geológica del Perú, 114, 20–48.

639   DeVries, T.J., Jud, N.A., 2018. Lithofacies patterns and paleogeography of the Miocene Chilcatay

640   and lower Pisco depositional sequences (East Pisco Basin, Peru). Boletín de la Sociedad Geológica

641   del Perú, Volumen Jubilar 8, 124–167.

642   DeVries, T.J., Urbina, M., Jud, N.A., 2017. The Eocene-Oligocene Otuma depositional sequence

643   (East Pisco Basin, Peru): Paleogeographic and paleoceanographic implications of new data. Boletín

644   de la Sociedad Geológica del Perú, 112, 14–38

645   Di Celma, C., Malinverno, E., Bosio, G., Collareta, A., Gariboldi, K., Gioncada, A., Molli, G.,

646   Basso, D., Varas-Malca, R.M., Pierantoni, P.P., Villa, I.M., Lambert, O., Landini, W., Sarti, G.,

647   Cantalamessa, G., Urbina, M., Bianucci, G., 2017. Sequence stratigraphy and paleontology of the

648   upper Miocene Pisco Formation along the western side of the lower Ica valley (Ica Desert, Peru).

649   Rivista Italiana di Paleontologia e Stratigrafia, 123, 255–274. https://doi.org/10.13130/2039-

650   4942/8373.

651   Di Celma, C., Malinverno, E., Bosio, G., Gariboldi, K., Collareta, A., Gioncada, A., Landini, W.,

652   Pierantoni, P.P., Bianucci, G., 2018a. Intraformational unconformities as a record of late Miocene

653   eustatic falls of sea level in the Pisco Formation (southern Peru). Journal of Maps, 14, 607–619.

654   https://doi.org/10.1080/17445647.2018.1517701.

655   Di Celma, C., Malinverno, E., Cantalamessa, G., Gioncada, A., Bosio, G., Villa, I.M., Gariboldi,

656   K., Rustichelli, A., Pierantoni, P.P., Landini, W., Tinelli, C., Collareta, A., Bianucci, G., 2016a.

657   Stratigraphic framework of the late Miocene Pisco Formation at Cerro Los Quesos (Ica Desert,

658   Peru). Journal of Maps, 12, 1020–1028. https://doi.org/10.1080/17445647.2015.1115783.

659   Di Celma, C., Malinverno, E., Collareta, A., Bosio, G., Gariboldi, K., Lambert, O., Landini, W.,

660   Gioncada, A., Villa, I.M., Coletti, G., Muizon, C. de, Urbina, M., Bianucci, G., 2018b. Facies

661   analysis, stratigraphy and marine vertebrate assemblage of the early Miocene Chilcatay Formation

662   at Ullujaya (Pisco basin, Peru). J. Maps 14, 257–268.

663   https://doi.org/10.1080/17445647.2018.1456490.

664   Di Celma, C., Malinverno, E., Gariboldi, K., Gioncada, A., Rustichelli, A., Pierantoni, P.P.,

665   Landini, W., Bosio, G., Tinelli, C., Bianucci, G., 2016b. Stratigraphic framework of the late

666   Miocene to Pliocene Pisco Formation at Cerro Colorado (Ica Desert, Peru). J. Maps 12, 515–557.

667   https://doi.org/10.1080/17445647.2015.1047906.

668   Di Celma, C., Pierantoni, P.P., Malinverno, E., Collareta, A., Lambert, O., Landini, W., Bosio, G.,

669   Gariboldi, K., Gioncada, A., Muizon, C. de, Molli, G., Marx, F.G., Varas-Malca, R.M., Urbina, M.,

670   Bianucci, G., 2019. Allostratigraphy and paleontology of the lower Miocene Chilcatay Formation in

671   the Zamaca area, East Pisco basin, southern Peru. J. Maps 15, 393–405.

672   https://doi.org/10.1080/17445647.2019.1604439.

673   Dunbar, R.B., Marty, R.C., Baker, P.A., 1990. Cenozoic marine sedimentation in the Sechura and

674   Pisco basins, Peru. Palaeogeogr. Palaeoclim. 77, 235–261.

675   Ehret, D.J., Hubbell, G., MacFadden, B.J. 2009. Exceptional preservation of the white shark

676   Carcharodon (Lamniformes, Lamnidae) from the early Pliocene of Peru. Journal of Vertebrate

677   Paleontology, 29, 1–13. https://doi.org/10.1671/039.029.0113.

678   Ehret, D.J., Macfadden, B.J., Jones, D.S., DeVries, T.J., Foster, D.A., Salas-Gismondi, R., 2012.

679   Origin of the white shark Carcharodon (Lamniformes: Lamnidae) based on recalibration of the

680   Upper Neogene Pisco Formation of Peru. Palaeontology, 55, 1139–1153.

681   https://doi.org/10.1111/j.1475-4983.2012.01201.x.

682   Elliott, J.C., 2002. Calcium phosphate biominerals. Reviews in Mineralogy and Geochemistry,

683   48(1), 427-453.

684   Elorza, J.; Astibia, H.; Murelaga, X.; Pereda-Suberbiola, X., 1999. Francolite as a diagenetic

685   mineral in dinosaur and other Upper Cretaceous reptile bones (Laño, Iberian Peninsula):

686   microstructural, petrological and geochemical features. Cretaceous Research 20: 169187.

687   doi:10.1006/cres.1999.0144.

688   Emeis, K.C., Whelan, J.K., Tarafa, M. 1991. Sedimentary and geochemical expressions of oxic and

689   anoxic conditions on the Peru shelf. Geological Society, London, Special Publications, 58(1), 155–

690   170.

691   Esperante, R., Brand, L., Nick, K.E., Poma, O., Urbina, M., 2008. Exceptional occurrence of fossil

692   baleen in shallow marine sediments of the Neogene Pisco Formation, Southern Peru. Palaeogeogr.

693   Palaeoclimatol. Palaeoecol. 257, 344–360.

694   Esperante, R., Brand, L.R., Chadwick, A.V., Poma, O., 2015. Taphonomy and paleoenvironmental

695   conditions of deposition of fossil whales in the diatomaceous sediments of the Miocene/Pliocene

696   Pisco Formation, southern Peru - a new Fossil-Lagerstätte. Palaeogeography Palaeoclimatology

697   Palaeoecology, 417, 337–370. https://doi.org/10.1016/j.palaeo.2014.09.029.

698   Gariboldi, K., Bosio, G., Malinverno, E., Gioncada, A., Di Celma, C., Villa, I.M., Urbina, M.,

699   Bianucci, G., 2017. Biostratigraphy, geochronology and sedimentation rates of the upper Miocene

700   Pisco Formation at two important marine vertebrate fossil-bearing sites of southern Peru.

701   Newsletters on Stratigraphy, 50, 417–444. https://doi.org/10.1127/nos/2017/0345.

702   Gariboldi, K., Gioncada, A., Bosio, G., Malinverno, E., Di Celma, C., Tinelli, C., Cantalamessa, G.,

703   Landini, W., Urbina, M., Bianucci, G., 2015. The dolomite nodules enclosing fossil marine

704   vertebrates in the East Pisco Basin, Peru: field and petrographic insights into the Lagerstätte

705   formation. Palaeogeography Palaeoclimatology Palaeoecology, 438, 81–95.

706   https://doi.org/10.1016/j.palaeo.2015.07.047, 2015.

707   Gioncada, A., Collareta, A., Gariboldi, K., Lambert, O., Di Celma, C., Bonaccorsi, E., Urbina, M.,

708   Bianucci, G., 2016. Inside baleen: exceptional microstructure preservation in a late Miocene whale

709   skeleton from Peru. Geology 44, 839–842.

710   Gioncada, A., Gariboldi, K., Collareta, A., Di Celma, C., Bosio, G., Malinverno, E., Lambert, O.,

711   Pike, J., Urbina, M., Bianucci, G., 2018a. Looking for the key to preservation of fossil marine

712   vertebrates in the Pisco Formation of Peru: new insights from a small dolphin skeleton. Andean

713   Geology 45, 379–398.

714   Gioncada, A., Petrini, R., Bosio, G., Gariboldi, K., Collareta, A., Malinverno, E., Bonaccorsi, E., Di

715   Celma, C., Pasero, M., Urbina, M., Bianucci, G., 2018b. Insights into the diagenetic environment of

716   fossil marine vertebrates of the Pisco Formation (late Miocene, Peru) from mineralogical and Sr-

717   isotope data. Journal of South American Earth Sciences, 81, 141-152.

718   https://doi.org/10.1016/j.jsames.2017.11.014.

719   Hampel, A., 2002. The migration history of the Nazca Ridge along the Peruvian active margin: A

720   re-evaluation and some geological implications. Earth and Planetary Science Letters, 203, 665–

721   679.Herwartz, D., Tütken, T., Jochum, K. P., Sander, P. M., 2013. Rare earth element systematics

722   of fossil bone revealed by LA-ICPMS analysis. Geochimica et Cosmochimica Acta, 103, 161–183.

723   https://doi.org/10.1016/j.gca.2012.10.038.

724   Hsu, J.T., 1992. Quaternary uplift of the Peruvian coast related to the subduction of the Nazca

725   Ridge: 13.5 to 15.6 degrees South latitude. Quaternary International 15/16, 87–97.

726   https://doi.org/10.1016/1040-6182(92)90038-4.

727   Hubert, J.F., Panish, P.T., Chure, D.J., Prostak, K.S. 1996. Chemistry, microstructure, petrology,

728   and diagenetic model of Jurassic dinosaur bones, Dinosaur National Monument, Utah. Journal of

729   Sedimentary Research, 66(3), 531-547.

730   Keenan, S.W., 2016. From bone to fossil: A review of the diagenesis of bioapatite. American

731   Mineralogist, 101, 1943–1951. https://doi.org/10.2138/am-2016-5737.

732   Keenan, S.W., Engel, A.S., 2017. Early diagenesis and recrystallization of bone. Geochimica et

733   Cosmochimica Acta, 196, 209–223. https://doi.org/10.1016/j.gca.2016.09.033.

734 Keenan, S.W., Engel, A.S., Roy, A., Bovenkamp-Langlois, G.L., 2015. Evaluating the

735 consequences of diagenesis and fossilization on bioapatitelattice structure and composition.

736 Chemical Geology, 413, 18–27.

737 Kim, J.H., Torres, M.E., Haley, B.A., Kastner, M., Pohlman, J.W., Riedel, M., Lee, Y.J. (2012).

738 The effect of diagenesis and fluid migration on rare earth element distribution in pore fluids of the

739 northern Cascadia accretionary margin. Chemical Geology, 291, 152–165.

740 Kowal-Linka, M., Jochum, K.P., Surmik, D., 2014. LA-ICP-MS analysis of rare earth elements in

741 marine reptile bones from the Middle Triassic bonebed (Upper Silesia, S Poland): Impact of long-

742 lasting diagenesis, and factors controlling the uptake. Chemical Geology, 363, 213–228.

743 Kulm, L.D., Resig, J.M., Thornburg, T.M., Schrader, H.J., 1982. Cenozoic structure, stratigraphy

744 928 and tectonics of the central Peru forearc. In: Legget, J.K. (Ed.), Trench and forearc geology:

745 sedimentation and tectonics on modern and ancient plate margins. London, Blackwells, 151–169.

746 https://doi.org/10.1144/GSL.SP.1982.010.01.10.

747 Lambert, O., Collareta, A., Landini, W., Post, K., Ramassamy, B., Di Celma, C., Urbina, M.,

748 Bianucci, G. 2015. No deep diving: evidence of predation on epipelagic fish for a stem beaked

749 whale from the Late Miocene of Peru. Proceedings of the Royal Society B: Biological Sciences,

750 282(1815), 20151530. https://doi.org/10.1098/rspb.2015.1530.

751 Lambert, O., Muizon, C. de, 2013. A new long-snouted species of the Miocene pontoporiid dolphin

752 Brachydelphis and a review of the Mio-Pliocene marine mammal levels in the Sacaco Basin, Peru.

753 Journal of Vertebrate Paleontology, 33, 709–721.

754 https://doi.org/10.1080/02724634.2013.74340513.743405.

755 León, W., Aleman, A., Torres, V., Rosell, W., de la Cruz, O. 2008. Estratigrafía, sedimentología y

756 evolución tectónica de la cuenca Pisco Oriental. Boletín INGEMMET, ser. D., 27, 1–144.

757 Li, Z., Pasteris, J.D., 2014. Chemistry of bone mineral, based on the hypermineralized rostrum of

758 the beaked whale Mesoplodon densirostris. American Mineralogist, 99, 645–653.

759 https://doi.org/10.2138/am.2014.4571

760 Macharé, J., Ortlieb, L., 1992. Plio-Quaternary vertical motions and the subduction of the Nazca

761 Ridge, central coast of Peru. Tectonophysics, 205, 97–108. https://doi.org/10.1016/0040-

762 1951(92)90420-B.

763 Manheim, F., Rowe, G.T., Jipa, D. 1975. Marine phosphorite formation off Peru. Journal of

764 Sedimentary Research, 45(1), 243–251. https://doi.org/10.1306/212F6D20-2B24-11D7-

765 8648000102C1865D

766 Marocco, R., Muizon, C. de, 1988a. Los vertebrados del Neogeno de la costa sur del Perú: ambiente

767 sedimentario y condiciones de fosilización. Bulletin de l'Institut Français d'études Andines, 17,

768 105–117.

769 Marocco, R., Muizon, C. de, 1988b. Le Bassin Pisco, bassin cénozoïque d'avant arc de la côte du

770 Pérou central: analyse géodynamique de son remplissage. Géodynamique, 3, 3–19.

771 Marx, F.G., Collareta, A., Gioncada, A., Post, K., Lambert, O., Bonaccorsi, E., Urbina, M.,

772 Bianucci, G., 2017a. How whales used to filter: exceptionally preserved baleen in a Miocene

773 cetotheriid. J. Anat. 231, 212–220.

774 McCoy, V.E., Young, R.T., Briggs, D.E.G., 2015. Sediment permeability and the preservation of

775 soft-tissues in concretions: An experimental study. Palaios, 30, 608–612.

776 Meister, P., Gutjahr, M., Frank, M., Bernasconi, S.M., Vasconcelos, C., McKenzie, J.A. 2011.

777 Dolomite formation within the methanogenic zone induced by tectonically driven fluids in the Peru

778 accretionary prism. Geology, 39(6), 563-566.

779 Michard, A., 1989. Rare earth element systematics in hydrothermal fluids. Geochimica et

780 Cosmochimica Acta, 53, 745–750. https://doi.org/10.1016/0016-7037(89)90017-3.

781 Muizon C. de., 1984. Les Vertébrés de la Formation Pisco (Pérou). Deuxième partie: Les

782 Odontocètes (Cetacea, Mammalia) du Pliocène inférieur de Sud-Sacaco. Travaux de l'Institut

783 Français d'Études Andines, 27, 1-188.

784 Muizon, C. de, 1988. Les Vertébrés de la Formation Pisco (Pérou). Troisième partie: Les

785 Odontocètes (Cetacea, Mammalia) du Miocène. Travaux de l'Institut Français d'Études Andines, 42,

786 1–244.

787 Muizon, C. de, Bellon, H., 1980. L'âge mio-pliocène de la Formation Pisco (Pérou). Comptes

788 Rendus Hebdomadaires des Séances de l'Académie des Sciences de Paris, Série D, 290, 1063–

789 1066.

790 Muizon, C. de, DeVries, T.J., 1985. Geology and paleontology of late Cenozoic marine deposits in

791 the Sacaco area (Peru). Geologische Rundschau, 74, 547–563. https://doi.org/10.1007/BF01821211.

792 Muramiya, Y., Yoshida, H., Kubota, K., Minami, M. 2020. Rapid formation of gigantic spherical

793 dolomite concretion in marine sediments. Sedimentary Geology, 105664.

794 North American Commission on Stratigraphic Nomenclature [NACSN], 2005. North American

795 stratigraphic code. AAPG (American Association of Petroleum Geologists) Bulletin, 89, 1547–

796 1591.

797 Olszta, M.J., Cheng, X., Jee, S.S., Kumar, R., Kim, Y.Y., Kaufman, M.J., Douglas, E.P., Gower,

798 L.B., 2007. Bone structure and formation: A new perspective. Materials Science and Engineering:

799 R: Reports, 58, 77–116. https://doi.org/10.1016/j.mser.2007.05.001.

800 Pasero, M., Kampf, A.R., Ferraris, C., Pekov, I.V., Rakovan, J., White, T.J., 2010. Nomenclature of

801 the apatite supergroup minerals. European Journal of Mineralogy, 22, 163–179.

802 https://doi.org/10.1127/0935-1221/2010/0022-2022.

803 Pilger, R.H., 1981. Plate reconstructions, aseismic ridges, and low-angle subduction beneath the

804 Andes. Geologica Society of America Bulletin, 92, 448–456. https://doi.org/10.1130/0016-

805 7606(1981)92<448:PRARAL>2.0.CO;2.

806 Pfretzschner, H.U., 2000a. Microcracks and fossilization of Haversian bone. Neues Jahrbuch für

807 Geologie und Paläontologie-Abhandlungen, 413–432.

808 Pfretzschner, H.U., 2000b. Pyrite formation in Pleistocene bones-a case of very early mineral

809 formation during diagenesis. Neues Jahrbuch für Geologie und Paläontologie-Abhandlungen, 143–

810 160.

811 Pfretzschner, H.U., 2001a. Pyrite in fossil bone. Neues Jahrbuch für Geologie und Paläontologie-

812 Abhandlungen, 1–23.

813 Pfretzschner, H.U., 2001b. Iron oxides in fossil bone. Neues Jahrbuch für Geologie und

814 Paläontologie-Abhandlungen, 417–429.

815 Pfretzschner, H.U., 2004. Fossilization of Haversian bone in aquatic environments. Comptes

816 Rendus Palevol, 3, 605–616. https://doi.org/10.1016/j.crpv.2004.07.006.

817 Rhoads, D.C., Mulsow, S.G., Gutschick, R., Baldwin, C.T., Stolz, J.F. 1991. The dysaerobic zone

818 revisited: a magnetic facies? Geological Society, London, Special Publications, 58(1), 187–199.

819 Shapiro, R.S., Spangler, E. 2009. Bacterial fossil record in whale-falls: petrographic evidence of

820 microbial sulfate reduction. Palaeogeography, Palaeoclimatology, Palaeoecology, 274(3-4), 196–

821 203.

822 Solís Mundaca, F.A., 2018. Bioestratigrafía e implicancias paleoceanográficas de las diatomeas de

823 la sección Cerro Caucato, Formación Pisco, Ica, Perù. Master Thesis, Universidad Peruana

824 Cayetano Heredia, Lima, Peru, 125 pp.

825 Thornburg, T.M., Kulm, L.D., 1981. Sedimentary basins of the Peru continental margin: structure,

826 stratigraphy, and Cenozoic tectonics from 6ºS to 16ºS latitude. In: Kulm, L.D., Dymond, J., Dasch,

827 E.J., Hussong, D.M. (Eds.), Nazca plate: crustal formation and Andean convergence. Geological

828 Society of America Memoir, 154, 393–422.

829 Trueman, C.N., Tuross, N., 2002. Trace elements in recent and fossil bone apatite. Reviews in

830 Mineralogy and Geochemistry, 48, 489–521. https://doi.org/10.2138/rmg.2002.48.13.

831 Trueman, C.N., Behrensmeyer, A.K., Tuross, N., Weiner, S., 2004. Mineralogical and

832 compositional changes in bones exposed on soil surfaces in Amboseli National Park, Kenya:

833 diagenetic mechanisms and the role of sediment pore fluids. Journal of Archaeological Science,

834 31(6), 721–739. https://doi.org/10.1016/j.jas.2003.11.003.

835 Trueman, C.N., 2013. Chemical taphonomy of biomineralized tissues. Palaeontology, 56(3), 475-

836 486. https://doi.org/10.1111/pala.12041

837 Trueman, C.N., Privat, K., Field, J., 2008. Why do crystallinity values fail to predict the extent of

838 diagenetic alteration of bone mineral? Palaeogeography, Palaeoclimatology, Palaeoecology, 266,

839 160–167. https://doi.org/10.1016/j.palaeo.2008.03.038.

840 Vietti, L.A., Bailey, J.V., Fox, D.L., Rogers, R.R., 2015. Rapid formation of framboidal sulfides on

841 bone surfaces from a simulated marine carcass fall. Palaios, 30(4), 327–334.

842 http://dx.doi.org/10.2110/palo.2014.027

843 Wopenka, B., Pasteris, J.D., 2005. A mineralogical perspective on the apatite in bone. Materials

844 Science and Engineering: C, 25, 131–143. https://doi.org/10.1016/j.msec.2005.01.008.

845 Zúñiga-Rivero, F.J., Klein, G.D., Hay-Roe, H., Álvarez-Calderon, E., 2010. The hydrocarbon

846 potential of Peru. Lima, BPZ.

847

848 **Figure captions**

849 **Figure 1. Bone structure and microstructure. A.** Bone structure in cross section. The bone tissue

850 can be distinguished into the outer compact bone and the inner cancellous bone. The compact bone

851 is an external layer composed by elemental units called osteons, at the center of which are the

852 Haversian canals that host blood vessels and nerves. The compact bone is covered by an outer

853 membrane called periosteum. The cancellous bone (trabecular or spongy bone) comprises the

854 internal tissue of the bone and it is formed by the trabeculae, elemental units that partition the inner

855 portion of the bone into intertrabecular medullary cavities where the bone marrow is stored. See the

856 schematic bioapatite unit of the bone tissue at the bottom right of the figure. **B.** Sketch illustrating

857 the main transformations that bone bioapatite undergoes during fossilization. The first step is the

858 loss of the OM (i.e., Organic Matter), which leaves pore spaces in which diagenetic fluids can

859 circulate. These fluids enriched in dissolved ions allow the replacement of Ca^{2+}, OH^-, PO_4^{3-} in the

860 apatite lattice, while favoring the recrystallization of apatite and precipitation of new apatite with

861 consequent reduction of porosity in the bone. Redrawn and modified after Keenan (2016).

862 **Figure 2. Geographical and paleontological setting. A.** Geographical setting of the East Pisco

863 Basin and Sacaco sub-basin in the Ica and Arequipa regions (Peru). **B.** Satellite image and positions

864 of the investigated localities of the East Pisco Basin: Cerro Colorado, Pampa Corre Viento, Cerro

865 los Quesos, Cerro la Bruja and Ullujaya, along the western side of the Ica River. **C.** Satellite image

866 and positions of the investigated localities of the Sacaco Basin: Hueso Blanco and Montemar near

867 Puerto Lomas. **D.** An investigated fossil specimen (CC-M11) of a mysticete baleen whale in the

868 desert environment of the Ica desert along the Peruvian coast.

869 **Figure 3. Examples of vertebrate bone types.** Fossil bones investigated in the Ica Desert have

870 been classified into six different types (1 to 6) based on their macroscopic characteristics (see Table

871 1).

872 **Figure 4. Bone photomicrographs. A.** Compact bone of the specimen CLQ-M3 (type 1b, see

873 Table 1) in transmitted plane-polarized light showing the preserved original microstructure (i.e.,

874 primary and secondary osteons, lamellae and osteocyte lacunae). **B.** Compact bone of the specimen

875 CLQ-M1 (type 1c) in reflected light, showing the preserved original microstructure (i.e., lamellae).

876 Note that the Haversian canals are filled by a sparry dolomitic cement. **C.** Compact bone of the

877 specimen MT-M1 (type 6) in transmitted plane-polarized light, showing preserved lamellae and

878 osteocyte lacunae, as well as pervasive fractures. In the bottom-left inset, osteocyte lacunae and

879 canaliculi filled with iron oxides are shown. Note the pervasive and polygonal microcracks cutting

880 the osteons, and the carbonate filling of the Haversian canals. **D.** Cancellous bone of the specimen

881 CLQ-M10 (type 1c) in transmitted plane-polarized light, showing microborings from bacterial

882 activity in the outer surface of the bone. Dolomite cement is present inside the microborings, in the

883 intertrabecular medullary cavities, and in the surrounding diatomaceous sediment. **E.** Cancellous

884 bone of the specimen CC-M22 (type 1c) exhibiting a very fragile bone tissue and sediment particles

885 (terrigenous grains and volcanic glasses) filling the bone cavities. These particles entered in the

886 bone cavities along with seawater, probably by being sucked in as a consequence of the escaping of

887 gas bubbles originated during decay of the organic matter. **F.** Compact bone of the specimen MT-

888 M1 (type 6) in transmitted cross-polarized light, showing the mosaic carbonate cement filling of the

889 Haversian canals precipitated during the late diagenesis. **G.** Cancellous bone of the specimen CC-

890 M11 (type 2), showing the bright red color of the bone visible both macroscopically and under the

891 microscope. Note that the intertrabecular medullary cavities are filled by Fe-oxides, the ghosts of

892 framboidal pyrite. Fe-oxides can fill the whole cavity or exhibit secondary filling in the center. **H.**

893 Detail of a blood vessel cavity of the specimen CC-M11 (type 2), exhibiting spherules of Fe-oxides,

894 the ghosts of framboidal pyrite, which strictly adhere to the bone tissue. The center of the cavity is

895 filled by secondary anhydrite.

896 **Figure 5. SEM-BSE images of fossil bones. A.** Compact bone of the specimen CC-M63 (type 1a)

897 exhibiting fragile and not permineralized bone tissue. Note the radial cracks around the osteons. **B.**

898 Compact bone of the specimen UL-O5 (type 4) exhibiting a moderately hard tissue. Note the cracks

899 that are present around the osteons, and that some Haversian canals in the center of the image are

900 partially filled by apatite. **C.** Close-up of the bone tissue and osteocyte lacunae of the specimen

901 UL-O5 (type 4) displaying a scarce permineralization. **D.** Close-up of a Haversian canal of the

902 specimen UL-O5 (type 4) displaying apatite filling, precipitated during fossilization. **E.** Compact

903 bone of the specimen MT-M1 (type 6), exhibiting a highly mineralized tissue. **F.** Compact bone of

904 the specimen CC-M28 (type 2), showing a highly mineralized tissue and brighter areas suggesting

905 Fe-oxide grains in the bone tissue. Note the different average atomic weight (different shades of

906 grey) in the diverse bone types, revealing a different degree of permineralization.

907 **Figure 6. SEM-BSE images of the cements filling the bone cavities. A.** Compact (external) and

908 cancellous (internal) bone of the mysticete specimen CLQ-M67. Note the dolomite filling the bone

909 cavities (both Haversian canals and intertrabecular medullary cavities) and the microborings, the

910 latter being referable to the "type C" (*sensu* Gariboldi et al. 2015). **B.** Close-up of a bone trabecula

911 of the odontocete specimen UL-O5. Note the different generations of dolomite (dark grey)

912 occurring near the bone tissue, and calcite in the center of the bone cavity. **C.** Close-up of a

913 framboidal Fe-oxide, ghost of a pyrite framboid, in the dolomite cement embedding and filling the

914 bone of the specimen CLQ-M67. **D.** Close-up of cancellous bone of the odontocete specimen UL-

915 O41, showing calcite cement filling the intertrabecular medullary cavities, with a fracture filled

916 secondarily by gypsum.

917 **Figure 7. EPMA compositional diagrams of bone apatite.** Values are shown as atoms per

918 formula unit.

919 **Figure 8. REE analyses on fossil bones.** REE spidergrams for four bone samples, volcanic ashes,

920 and diatomaceous sediments of the Lagerstätte. The REE patterns of seawater at different depths are

921 also shown. All data are normalized to the PAAS.

922 **Figure 9. $(La/Yb)_N$ vs $(La/Sm)_N$ of the analyzed bones compared to the REE ratios in**

923 **seawater.** Paths produced by processes acting in early and protracted diagenesis and metamorphism

924 are also indicated.

925 **Figure 10. Processes and factors acting during the post-mortem history of a whale.** Scheme of

926 the processes and factors that affect bones from the fall of the whale carcass to its complete burial

927 and later exposure in a modern desert environment (inspired by Keenan, 2016).

928 **Figure 11. Bone type processes and characterization.** Scheme of the processes that take place

929 during burial, early and late diagenesis, and exposure in a modern desert environment, with the

930 bone characterization for each bone type identified in the Pisco-Sacaco Fossil-Lagerstätte.

931

932 **Table captions**

933 **Table 1.** Fossil bone types obtained on the basis of macroscopic characteristics (color and relative

934 hardness, sediment type and presence of concretions) observed in East Pisco and Sacaco fossil

935 bones.

936 **Table 2.** Mean, number of analyses (in brackets) and standard deviation (SD) of the electron

937 microprobe analyses of bone, for the different types individuated in this work; bdl: below detection

938 limit; FeOtot: all Fe as FeO. Formula recalculated based on 13 total anions and 1 (F, Cl, OH). M

939 sites with 1+ and 2+ cations and T sites with 4+, 5+ and 6+ cations (Pasero et al., 2010).

940 **Table 3.** Trace element chemical composition of fossil bones and sediment samples, obtained by

941 means of ICP-MS. "A" stands for cortical bone, "B" for diatomaceous sediment, and "C" for

942 volcanic ash; bdl: below detection limit; nd: not determined.

943

944 **Supplementary Material**

945 **Table S1.** Complete dataset of the fossil bones analyzed for this work in the East Pisco Basin and

946 Sacaco sub-basins. Hueso Blanco and Montemar are localities from the Sacaco area. All the other

947 localities are from the Ica River Valley.

948 **Table S2.** Complete dataset of electron microprobe analyses of fossil bones. See text for analytical

949 details.

950

951

952 **Table 1**

Type	Description		Representative samples and *specimen****	Host sediment	Mineral cement or concretion
	color	hardness*			
1	white/pinkish	low hardness	1a: 11 [*CC-M63*]	1a: diatomaceous silt	dolomite concretion
		low hardness, fragile	1b: 2 [*CLQ-M3*]	1b: tephra	no dolomite concretion
		low hardness, easily crumbling	1c: M1A [*CLQ-M1*], M10A [*CLQ-M10*], M50A [*CLQ-M50*], CCA86 [*CC-M22*]	1c: diatomaceous silt/mudstone	variable development of dolomite concretion
2	red	moderately hard, fragile	12, 30 [*CC-M28*]	diatomaceous silt/sand, deformed by the load of the carcass	no concretion, but a Mn-Fe boundary is visible under the specimen (Fig. 3)
3	dark amber	moderately hard	3a: CCB86 [*CC-P7*]	silt/sand	specimen in a scarcely cemented nodule, no dolomite
4	pearly white	moderately hard	37 [*UL-O41*], 48 [*UL-O5*], D12 [*UL-O66*]	siliciclastic sand with carbonatic fraction	no
5	white/gray-white	hard/very hard	49 [*HB-1*], 51 [*HB-3*]	sand	no
6	dark gray	very hard	52 [*MT-M1*]	sand	no

* relative hardness, comparative estimation

**specimen to which the bone samples belong is in square brackets; details can be found in Table S1

953 **Table 2**

	Type 1		Type 2		Type 3a		Type 3b		Type 4		Type 5		Type 6	
	mean [5]	SD	mean [12]	SD	mean [14]	SD	mean [9]	SD	mean [14]	SD	mean [7]	SD	mean [4]	SD
SiO_2 wt%	0.11	0.12	1.12	0.49	2.45	1.12	0.01	0.01	0.01	0.01	bdl	0.01	0.01	0.01
MgO	0.49	0.11	2.53	1.32	1.81	0.22	1.09	0.09	0.37	0.10	0.64	0.32	0.53	0.05
CaO	45.14	2.38	32.12	4.21	40.59	2.28	47.92	0.80	47.97	2.26	47.88	3.31	50.89	0.27
MnO	0.01	0.02	0.12	0.03	0.09	0.03	0.09	0.02	0.02	0.02	0.02	0.02	0.02	0.02
FeOtot	0.04	0.03	17.32	6.96	4.55	1.42	0.10	0.03	0.05	0.11	0.04	0.04	0.08	0.05
Na_2O	1.37	0.17	1.30	0.30	1.06	0.17	1.10	0.07	1.28	0.16	1.25	0.07	0.91	0.10
SrO	0.13	0.05	0.07	0.08	0.13	0.05	0.13	0.05	0.13	0.09	0.04	0.04	0.22	0.11
PbO	bdl	-	0.01	0.02	bdl	-	bdl	-	bdl	-	bdl	-	0.01	0.02
P_2O_5	31.48	0.76	27.28	2.51	33.14	0.90	34.74	0.59	32.93	1.31	33.82	2.33	31.01	0.36
SO_3	2.78	0.23	2.74	0.53	2.64	0.35	3.31	0.08	3.00	0.26	2.82	0.38	2.06	0.51
F	1.41	0.27	1.36	0.25	1.58	0.41	3.40	0.59	2.29	0.42	2.39	0.63	1.95	0.32
Cl	0.86	0.21	0.87	0.38	0.67	0.21	0.12	0.03	0.42	0.29	0.35	0.15	0.33	0.07
H_2O_{calc}	0.59		0.57		0.66		0.00		0.36		0.35		0.51	
Total	84.42		87.42		89.38		92.01		88.86		89.60		88.53	

Formula proportions based on 13 total anions and 1 (F, Cl, OH)

Si	0.011		0.116		0.232		0.001		0.001		0.000		0.001	
Mg	0.074		0.392		0.259		0.150		0.053		0.091		0.078	
Ca	4.889		3.578		4.114		4.742		4.950		4.878		5.379	
Mn	0.001		0.011		0.007		0.007		0.002		0.002		0.002	
Fe	0.004		1.506		0.360		0.008		0.004		0.003		0.007	
Na	0.269		0.262		0.194		0.197		0.239		0.230		0.174	
Sr	0.008		0.004		0.007		0.007		0.007		0.002		0.013	
Pb	0.000		0.000		0.000		0.000		0.000		0.000		0.000	
P	2.694		2.401		2.654		2.717		2.685		2.722		2.590	
S	0.211		0.214		0.187		0.229		0.217		0.201		0.153	
F	0.451		0.447		0.473		0.993		0.698		0.719		0.608	
Cl	0.147		0.153		0.107		0.019		0.069		0.056		0.055	
OH	0.401		0.398		0.419		0.000		0.233		0.225		0.336	
M site	5.244		5.754		4.938		5.111		5.255		5.206		5.653	
T site	2.916		2.732		3.073		2.947		2.903		2.924		2.744	
Ca/P	1.81		1.49		1.55		1.75		1.84		1.79		2.08	

954

955

956

957 **Table 3**

Sample	11	30-01	ESP-2	52	CLQ20-Q	CLQ20-P	CLQ20-N	CLQT8-T4	CLQT8-base	CLQT8-T6	CLQT8-tephra
material	A	A	A	A	B	B	B	B	B	B	C
Li	1.53	4.00	2.59	1.66	52	48	23.9	3.9	20.9	7.9	0.64
Be	0.48	3.05	0.31	2.50	0.68	0.66	0.93	2.90	0.86	2.75	3.32
Ga	1.04	1.26	1.05	1.38	10.0	9.6	9.9	13.9	10.5	14.0	14.8
Rb	0.58	1.97	0.78	0.67	56	50	48	116	58	115	139
Sr	758	551	1060	1423	155	169	217	100	663	100	78
Y	7.4	235	4.2	21.5	4.6	4.5	8.6	12.3	5.0	12.2	13.4
Zr	11.0	22.1	33.0	87	68	67	94	120	66	118	128
Nb	0.34	0.44	0.31	0.44	5.5	5.1	6.0	12.9	5.7	12.4	14.5
Mo	2.92	51	9.7	2.60	5.9	5.5	4.1	5.2	66	5.8	2.96
Cs	0.03	0.14	0.03	0.07	5.1	4.5	3.6	4.3	4.9	4.7	4.3
Ba	27.5	52	49	81	219	206	315	734	504	683	785
La	5.0	5.7	1.00	4.0	9.8	10.4	15.6	47	24.0	43	52
Ce	7.7	8.2	1.28	4.4	17.5	18.3	29.6	86	51	78	95
Pr	0.84	1.10	0.17	0.40	2.01	2.11	3.5	8.7	5.8	8.0	9.7
Nd	3.22	4.8	0.88	1.46	7.1	7.4	13.0	27.5	18.4	25.3	30.0
Sm	0.62	1.34	0.23	0.42	1.16	1.22	2.30	3.9	2.01	3.8	4.2
Eu	0.12	0.38	0.06	0.12	0.29	0.29	0.56	0.60	0.44	0.58	0.60
Gd	0.74	4.7	0.38	1.01	0.93	0.90	1.83	2.40	1.03	2.29	2.43
Tb	0.11	0.75	0.06	0.19	0.14	0.13	0.27	0.38	0.16	0.36	0.39
Dy	0.73	6.7	0.47	1.60	0.82	0.83	1.56	2.23	0.92	2.08	2.30
Ho	0.17	2.43	0.13	0.44	0.17	0.16	0.31	0.43	0.18	0.40	0.45
Er	0.51	9.5	0.45	1.64	0.49	0.48	0.85	1.23	0.52	1.15	1.28
Tm	0.08	1.40	0.06	0.30	0.08	0.07	0.12	0.19	0.08	0.18	0.20
Yb	0.48	8.5	0.39	2.22	0.50	0.47	0.79	1.27	0.52	1.15	1.35
Lu	0.08	2.02	0.08	0.39	0.08	0.07	0.12	0.19	0.08	0.18	0.21
Hf	0.09	0.16	0.37	0.40	2.14	2.10	2.6	4.0	1.97	3.7	4.2
Ta	0.01	0.03	bdl	0.01	0.39	0.40	0.45	1.13	0.43	1.04	1.24
W	0.41	0.89	0.18	0.34	0.66	0.64	0.60	1.02	0.67	0.98	1.07
Pb	bdl	3.7	4.1	5.0	6.6	7.0	10.3	24.0	22.9	23.0	23.2

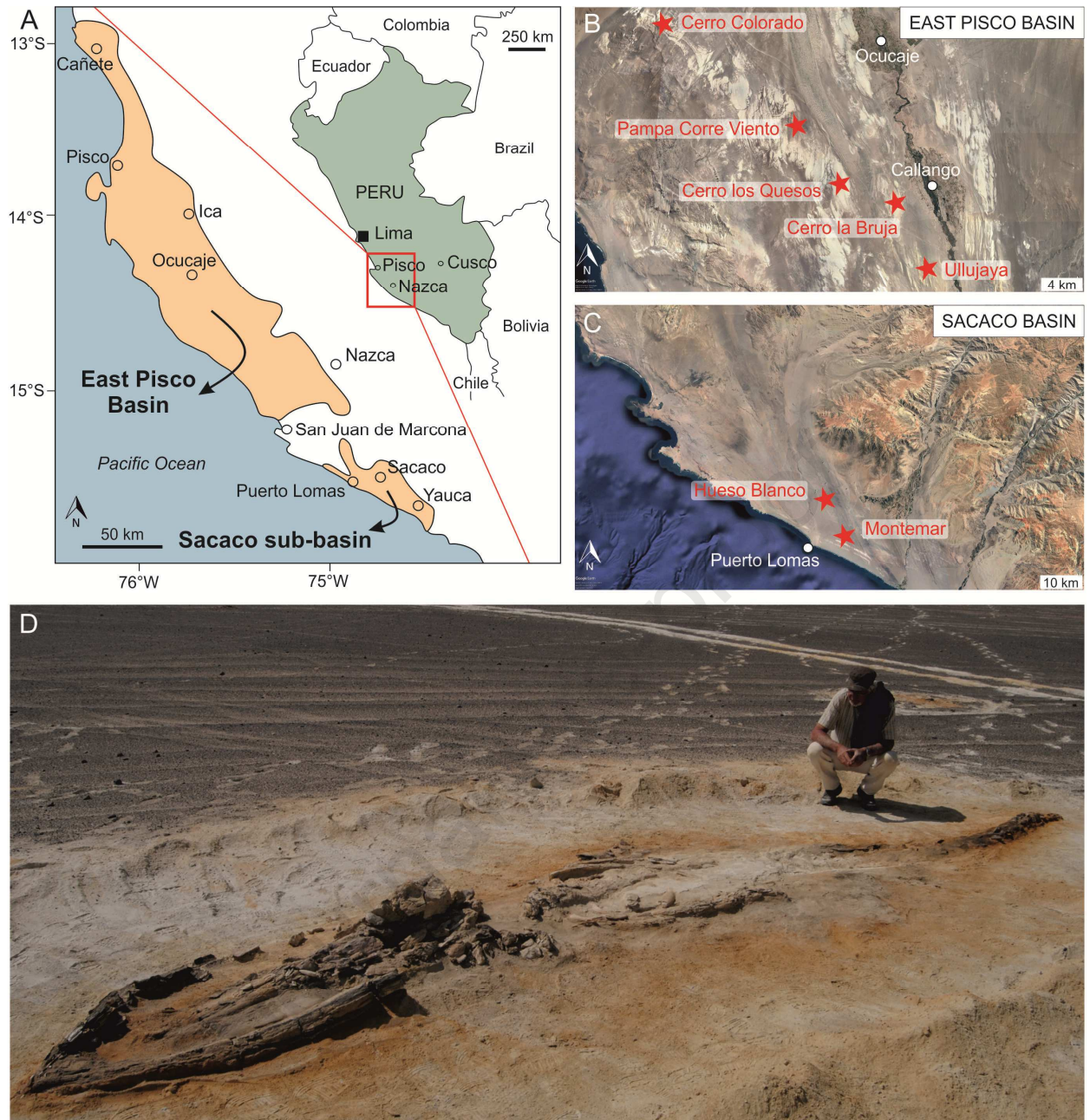|											
Th	0.29	0.34	0.04	0.11	4.5	4.5	4.6	19.4	7.2	17.9	22.1
U	7.7	24.0	1.46	250	2.00	1.96	1.63	4.8	4.9	4.9	4.9
Sc	0.97	1.39	1.83	2.50	4.3	4.9	4.3	3.8	4.4	5.3	2.7
V	3.3	29.7	13.2	28.1	87	112	63	22.2	109	45	5.2
Cr	4.2	14.0	7.4	9.3	47	42	23.2	10.6	65	24.9	4.7
Co	1.74	19.4	3.6	1.28	8.5	11.0	6.5	1.09	3.28	1.66	0.46
Ni	2.19	121	42	1.49	100	105	44	4.9	19.2	8.5	2.42
Cu	nd	32.4	14.8	421	21.7	31.4	20.6	5.1	37	14.1	nd
Zn	38	451	145	102	555	322	326	41	139	137	45

958

959

960

961

Figure 1

962

963

964

965

Figure 2

966

967

Type 1

CC-M22: cranium and articulated mandibles of small baleen whale (Cetotheriidae) from Pisco Fm, Cerro Colorado (East Pisco Basin)

Note the dolomite concretion originally fully embedding the fragile and white bones

Type 2

CC-M28: articulated skeleton of small baleen whale (Cetotheriidae) from Pisco Fm, Cerro Colorado (East Pisco Basin)

Note the red bones embedded in the diatomaceous silt reddened near the skeleton

Type 3

MUSM 887: partially articulated skeleton of small dolphin (*Brachydelphis mazeasi*) from Pisco Fm, Pampa Corre Viento (East Pisco Basin)

Note the dark and well mineralized bones delimited by a black boundary layer in yellowish sand

Type 4

UL-81(MUSM 2527): cranium of longirostral dolphin (*Chilcacetus cavirhinus*) from Chilcatay Fm, Ullujaya (East Pisco Basin)

Note the pearly white bones inside well consolidated grey sand

Type 5

HB-3: rib fragment of indeterminate cetacean from Pisco Fm, Hueso Blanco (Sacaco sub-basin)

Note the eroded white bone exposed in the desertic environment

Type 6

MT-M1: fragment of an isolated rib of indeterminate cetacean from Pisco Fm, Montemar (Sacaco sub-basin)

Note the dark color of the well mineralized bone

968

969

Figure 3

970

971

972

Figure 4

973

974

Figure 5

975

976

977

978   **Figure 6**

979

Figure 7

Figure 8

Figure 9

989

A   PRE-BURIAL

Processes

- disarticulation
- mechanical abrasion
- chemical corrosion
- encrustation by invertebrates
- scavenging by macrofauna
- bioerosion and microborings
(invertebrates, bacteria)

Factors

I. Carcass characteristics

- presence of soft tissues
- body dimension
- lipid content
- bone structure

II. Sea bottom environment

- oxic/suboxic/anoxic conditions
- hydrodinamism
- benthic and nectobenthic fauna
- pH conditions
- decaying organic matter

III. Type of sediment

- porosity and permeability
- possibility of foundering
- rate of sedimentation

B   BURIAL

Early Diagenesis   time ⟶   Late Diagenesis

Processes

- bone distortion
- permineralization
- mineral dissolution and recrystallization (apatite)
- dolomite filling of the bone cavities
- dolomite nodule formation
- pyrite formation

Factors

I. Porewater
conditions

- organic matter content
in the sediment
- primary permeability
- pH conditions
- Eh conditions

Processes

- gypsum/anhydrite precipitation
- late calcite precipitation
- Mn oxides precipitation
- formation of microcracks

Factors

I. Fluid circulation
- presence of
brines
- rock secondary
permeability

II. Compaction
- lithostatic
pressure

C   EXPOSURE

Processes

- weathering
(wind, humidity)
- Mn oxides
precipitation
- evaporitic mineral
crusts
- bleaching of cortical
bone tissue

Factors

I. Desert
environment

- wind strenght
- air/soil humidity
- thermal daily
excursion

II. Exposure time

990

991   **Figure 10**

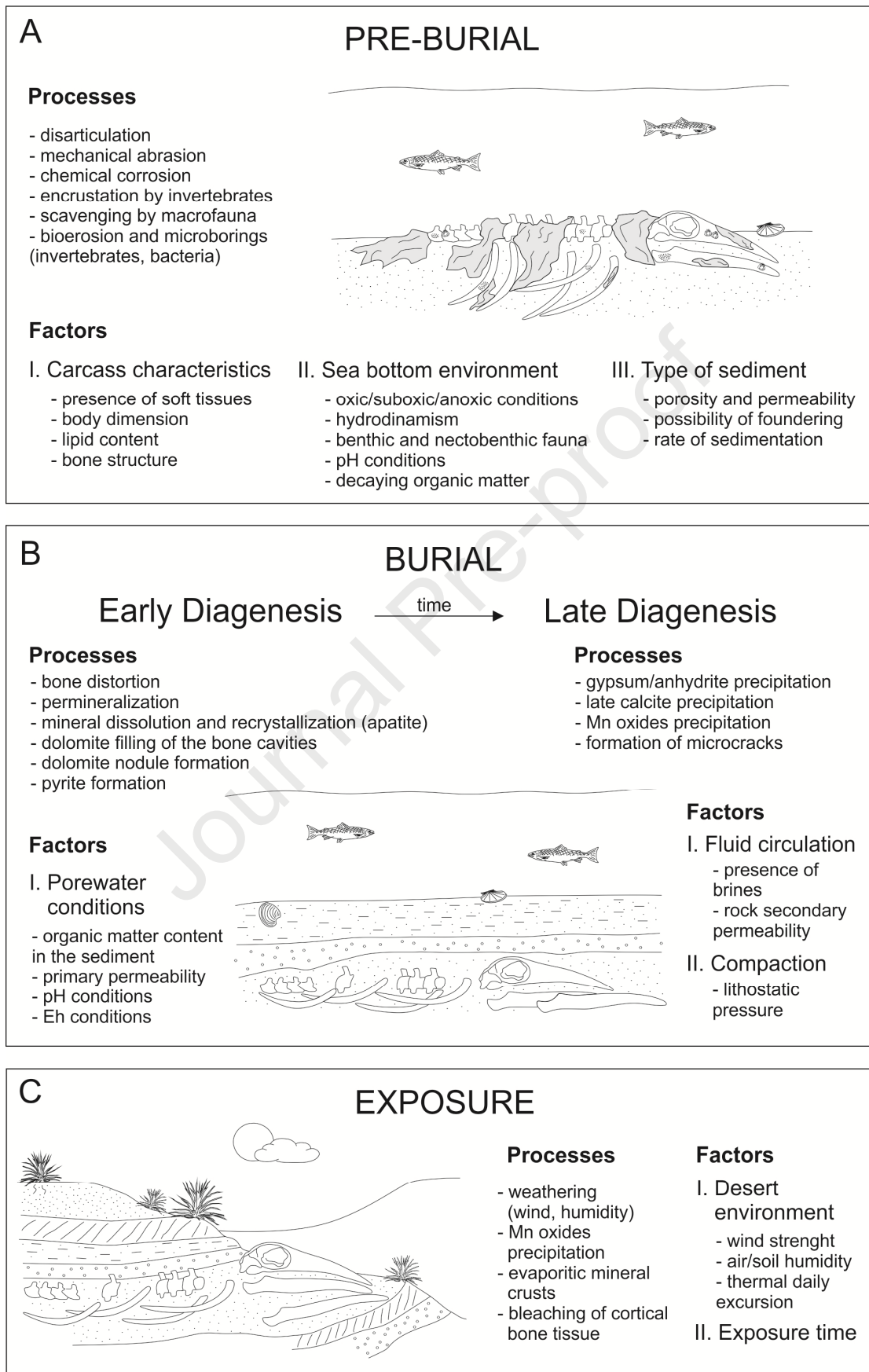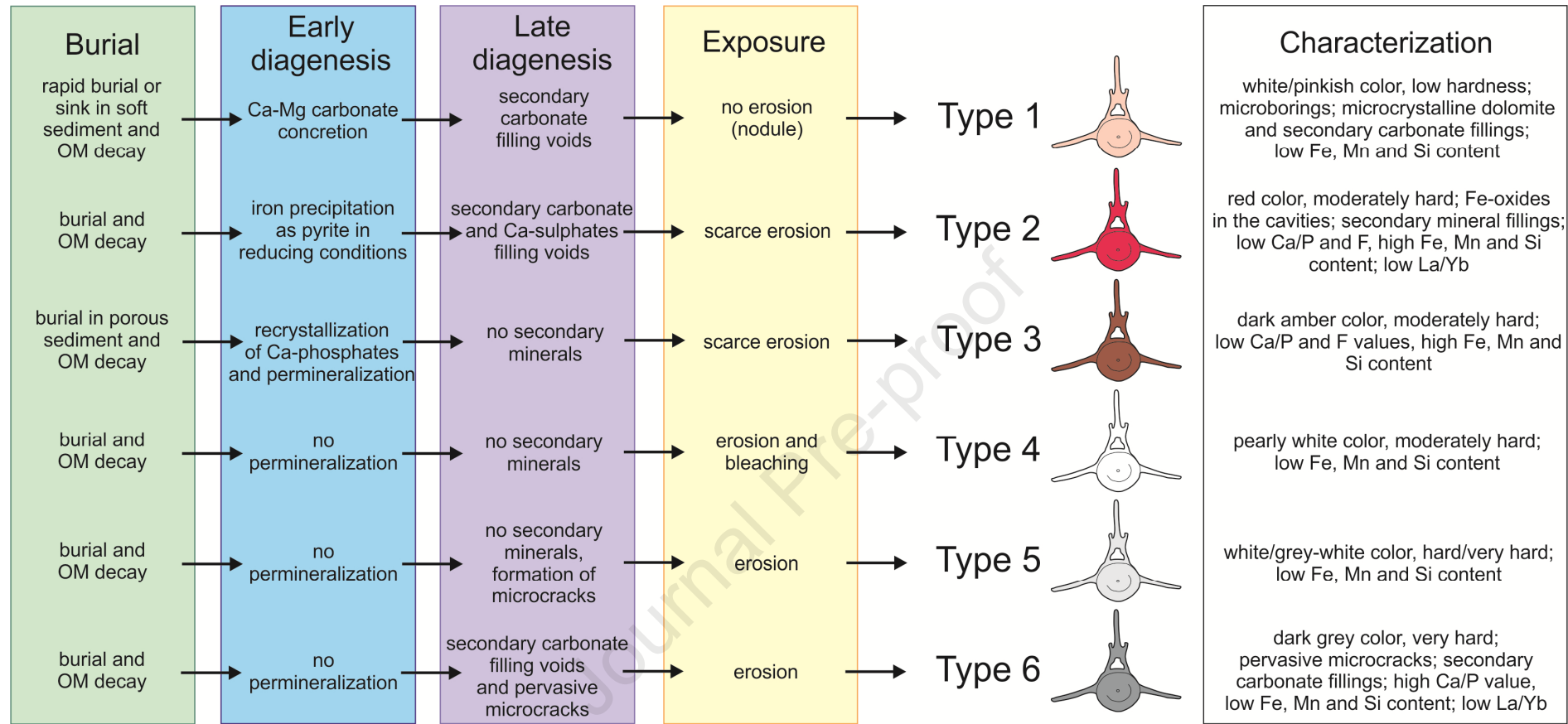| Burial	Early diagenesis	Late diagenesis	Exposure		Characterization
rapid burial or sink in soft sediment and OM decay	Ca-Mg carbonate concretion	secondary carbonate filling voids	no erosion (nodule)	Type 1	white/pinkish color, low hardness; microborings; microcrystalline dolomite and secondary carbonate fillings; low Fe, Mn and Si content
burial and OM decay	iron precipitation as pyrite in reducing conditions	secondary carbonate and Ca-sulphates filling voids	scarce erosion	Type 2	red color, moderately hard; Fe-oxides in the cavities; secondary mineral fillings; low Ca/P and F, high Fe, Mn and Si content; low La/Yb
burial in porous sediment and OM decay	recrystallization of Ca-phosphates and permineralization	no secondary minerals	scarce erosion	Type 3	dark amber color, moderately hard; low Ca/P and F values, high Fe, Mn and Si content
burial and OM decay	no permineralization	no secondary minerals	erosion and bleaching	Type 4	pearly white color, moderately hard; low Fe, Mn and Si content
burial and OM decay	no permineralization	no secondary minerals, formation of microcracks	erosion	Type 5	white/grey-white color, hard/very hard; low Fe, Mn and Si content
burial and OM decay	no permineralization	secondary carbonate filling voids and pervasive microcracks	erosion	Type 6	dark grey color, very hard; pervasive microcracks; secondary carbonate fillings; high Ca/P value, low Fe, Mn and Si content; low La/Yb

992

993

Figure 11

Declaration of interests

The authors declare that they have no known competing financial interests or personal relationships that could have appeared to influence the work reported in this paper.